Aging drives cerebrovascular network remodeling and functional changes in the mouse brain

Hannah C. Bennett[1,7], Qingguang Zhang[2,3,7], Yuan-ting Wu[1,4,7], Steffy B. Manjila[1,7], Uree Chon[1,5], Donghui Shin[1], Daniel J. Vanselow[1], Hyun-Jae Pi[1], Patrick J. Drew[2,6], Yongsoo Kim[1,2,8]

[1] Department of Neural and Behavioral Sciences, The Pennsylvania State University, Hershey, PA, 17033, USA
[2] Center for Neural Engineering, Department of Engineering Science and Mechanics, The Pennsylvania State University, University Park, PA, 16802, USA
[3] Department of Physiology, Michigan State University, East Lansing, MI 48824
[6] Department of Biomedical Engineering, Biology, and Neurosurgery, The Pennsylvania State University, University Park, PA, 16802, USA
[7] Equal contribution
[8] Lead contact. Email: yuk17@psu.edu

Current address:
[4]Department of Neurosurgery, Department of Computational Biomedicine, Cedars-Sinai Medical Center, CA 90048
[5]Stanford University, Stanford, CA 94305

Abstract

Aging is the largest risk factor for neurodegenerative disorders, and commonly associated with compromised cerebrovasculature and pericytes. However, we do not know how normal aging differentially impacts the vascular structure and function in different brain areas. Here we utilize mesoscale microscopy methods (serial two-photon tomography and light sheet microscopy) and *in vivo* imaging (wide-field optical spectroscopy and two-photon imaging) to determine detailed changes in aged cerebrovascular networks. Whole-brain vascular tracing showed an overall ~10% decrease in vascular length and branching density with ~7% increase in vascular radii in aged brains. Light sheet imaging with 3D immunolabeling revealed increased arteriole tortuosity of aged brains. Notably, vasculature and pericyte densities showed selective and significant reductions in the deep cortical layers, hippocampal network, and basal forebrain areas. We also found a significant increase in blood extravasation, implying compromised blood-brain barrier function in aged brains. Moreover, *in vivo* imaging in awake mice identified a reduction of baseline and on-demand blood oxygenation despite relatively intact neurovascular coupling. Collectively, we uncover regional vulnerabilities of cerebrovascular network and physiological changes that can mediate cognitive decline in normal aging.

Key Words:
Aging, pericyte, cerebrovasculature, brain, high-resolution mapping, serial two-photon tomography, light sheet fluorescence microscopy, neurovascular coupling

Highlight

- Brain-wide mapping of vasculature and pericyte changes with normal aging

- Simplified vascular network with tortuous vessels in aged brains
- Vascular rarefication in the deep cortical layers, hippocampus, and the basal forebrain
- Intact neurovascular coupling but lower blood oxygenation in aged animals

Introduction

Aging is the primary risk factor for the development of various neurodegenerative diseases. Notably, aging is associated with decreased cerebral blood flow and general vascular impairment [1]. A common denominator in diseases that increases the risk of dementia, such as stroke, atherosclerosis, and diabetes mellitus, is vascular perturbation and dysfunction of neurovascular coupling [2–9]. All of the disease processes mentioned above increase the risk of developing vascular dementia, which is the second leading cause of cognitive impairment in the United States. Impairment in the cerebrovascular network can have a significant impact on energy supply and metabolic waste removal processes, which can result in neuronal death linked with various clinical symptoms [10–12]. Thus, understanding the anatomical and functional changes in the brain vasculature upon normal aging is a critical first step in understanding neurodegenerative disorders.

The vessels of the cerebrovascular network are composed of endothelial cells linked by tight junctions. These blood vessels are surrounded by mural cells, such as vascular smooth muscle cells and pericytes, which wrap around vessels of the vascular tree and contribute to blood flow regulation [13]. Pericytes are essential for maintaining the blood brain barrier and play important roles in waste removal and capillary blood flow regulation [14–16]. The importance of these vascular cell types is becoming increasingly recognized in the context of brain disorders, particularly in the case of neurodegenerative diseases. Previous studies have shown that aging with cognitive impairment is associated with vascular pathologies including increased arterial tortuosity, rarefaction of the vascular tree, and impairment of pericyte dynamics [3,5,14,17–19]. In addition to anatomical changes, advanced aging is associated with reduced cerebral blood flow (CBF), increased CBF pulsatility, and stiffening of the major arteries [20–22]. It is becoming increasingly recognized that disruption to the brain's vasculature may precede the neuronal damage associated with neurodegenerative disease and other types of dementia [23], implying that vascular dysfunction may play a causative role in neurodegeneration. Despite its significance, it remains unclear how the cerebrovascular network and mural cell types across different brain regions undergo structural and functional changes during the aging process. Prior work has primarily focused on single brain regions without accounting for brain-wide changes in the cerebrovascular network, largely due to the complexities of visualizing and analyzing large 3D brain volumes.

Recent advances in 3D whole brain imaging methods make it possible to quantitatively examine detailed cerebrovascular networks in the entire mouse brain [24–29]. We previously showed that regional differences in pericyte density and cerebrovascular structure strongly correlate with the number of parvalbumin-expressing neuron populations in the cortex of young adult (2-month-old) mice [29]. Here, leveraging high-resolution 3D mapping methods (light sheet and serial two-photon microscopy), we ask whether there are regional vulnerabilities within the cerebrovasculature and mural cell types upon aging at 18 months (early aging), and 24-month-old (late aging) following the JAX Lifespan as biomarker criteria [30]. 24 months of age was deemed as late aging without a significant death rate, as mouse survivorship steadily declines after 24 months old [30]. We found selective reduction of vascular length and pericyte density in deep cortical layers, as well as the basal forebrain areas where cholinergic neurons with large cell bodies reside. Aging also causes vascular remodeling with increased arterial tortuosity in the

isocortex and reduces capillary pericyte density in the entorhinal cortex. In addition to anatomical changes, *in vivo* imaging (two-photon and wide field optical intrinsic signal imaging) of the vasculature in awake aged mice indicates low blood oxygenation at baseline and evoked conditions. Collectively, our results demonstrate significant cerebrovascular network changes, linked to regional vulnerabilities and reduced hemodynamic responsiveness in aging.

Results

Early aging in the mouse brain shows overall decreased vascular length density and branching density, but increased vascular radii

To determine structural changes of the cerebrovasculature upon normal aging, we applied our cerebrovascular mapping pipelines in 18-month-old (aged) mice in order to compare 2-month-old (young adult) mice [29] (Figure 1). We labeled the brain vasculature by cardiac perfusion of fluorescein isothiocyanate (FITC)-conjugated albumin gel [27,29,31,32]. Then, we utilized serial two-photon tomography (STPT) imaging to image the whole mouse brain at 1x1x5 µm resolution (*x,y,z;* media-lateral, dorsal-ventral, rostral-caudal) followed by computational analysis for vasculature tracing and quantification [29,33]. All signals were registered to the Allen Common Coordinate Framework (AllenCCF) as a reference brain [34] (Figure 1).

To identify potential regional vascular vulnerabilities, we first examined the overall changes of the cerebrovasculature across the whole mouse brain, comparing 18-month-old mice to 2-month-old mice (Figure 2A). Total vessel length in most regions remained similar between 18- and 2-month-old mice (Figure 2B) but overall brain volume increased about 6% (Figure 2C; not statistically significant). The brain volume increase was also seen with *in vivo* longitudinal MRI [35], indicating our result is not an artifact from fixation or imaging. As a result, overall vascular length density across different brain regions decreased by 5 – 10% in the aged brain (Figure 2D). In addition, we found an approximate 10-20% decrease in branching density across most brain regions (Figure 2E; Supplementary Data 1). In contrast, the average radius of 18-month-old mouse brain vasculature is increased by about 5 – 10% compared to 2-month-old mice, suggesting reduced basal constrictive tone (Figures 2F; Supplementary Data 1). Notably, we found significant changes in brain regions related to memory processing and storage (e.g., Ammon's horn; CA, lateral entorhinal cortex; ENTl, Anteromedial nucleus; AM), appetitive behavior (e.g., medial preoptic area; MPO, ventral premammillary area; PMv), body physiology and sleep (e.g., lateral preoptic area; LPO, anterior hypothalamic area; AHA), attention (e.g., substantia innominata; SI, medial septum; MS as basal forebrain areas), sensory processing and integration (e.g., zona incerta; ZI, Dorsal lateral geniculate nucleus; LGd), and executive function (e.g., medial group of the dorsal thalamus; MED) (Figure 2D-F, highlighted with magenta boxes; Supplementary Data 1).

Next, we examined isocortical areas for aging-related vascular changes. Surprisingly, isocortical areas showed no significant changes, with mostly less than 10% decrease in length and branching density, and about 5% increase in average vessel radius (Figure 2G-I). To examine vascular changes in the isocortex more intuitively, we utilized our previously developed isocortical flatmap with five distinct cortical domains marked by different colors (Figure 2J) [29]. We found a significant reduction in vessel length density only in layer 6 of aged brains compared to young brains (Figure 2K-N). Moreover, we quantified the nearest neighbor distance to vessels as a metric to access blood supply and found a significant increase only in layer 6 in 18-month-old mouse brain (Supplementary Figure 1). Our result corroborates a previous finding showing selective vulnerability of deep cortical layers to aging [36,37]. Together, these findings indicate that the vasculature of the isocortex is relatively resilient to aging, and the earliest evidence of age-related vascular degeneration occurs in layer 6.

Pericyte density in aged brains showed significant decrease in basal forebrain regions and the deep cortical layer.

150 Pericytes are a mural cell type that plays a key role in the regulation of the capillary
151 network blood flow and diameter and are known to be vulnerable in aging [15,16,38,39]. Our results
152 show increased vascular radius in aged brains, which raises the possibility of dysfunction in
153 pericytes in the maintenance of vascular diameter. To quantitatively determine changes of
154 pericytes, we compared capillary pericyte densities in 2-month-old and 18-month-old PDGFRβ-
155 Cre;Ai14 mice [40,41], where tdTomato is expressed in pericytes and other mural cells. We used
156 STPT imaging of PDGFRβ-Cre;Ai14 mice with previously developed computational analyses to
157 image, identify, and quantify changes of capillary pericytes upon aging across the whole mouse
158 brain [29,33] (Figure 1 bottom and Figure 3A).
159 Overall, pericyte density in the aged brain remained within 10% of that in young brains in
160 most areas, including many cortical and thalamic subregions (Figure 3B; Supplementary Data 2).
161 However, a significant reduction of pericyte density was found in basal forebrain areas (e.g., the
162 substantia innominata; SI, magnocellular nucleus; MA) and the closely related anterior amygdala
163 area (AAA) (Figures 3B; red boxed, C-D) [42]. Considering the basal forebrain contains cortical-
164 projecting cholinergic neurons, the observed significant reduction in pericyte and vascular
165 densities reflects the selective and early vulnerability of the basal forebrain during aging. These
166 results could potentially provide a link between known vascular impairment and dysfunction of
167 cholinergic neurons in neurodegenerative diseases such as Alzheimer's disease [43,44].
168 Given that we saw few vascular changes with aging in the isocortex (Figure 2), we
169 investigated whether this resilience extends to pericyte density. We compared 2-month- and 18-
170 month-old mice capillary pericyte densities by brain region using our isocortical flatmap (Figure
171 3E). The capillary pericyte density in aged mice overall remained similar to, or even slightly
172 increased as compared with young adult mice (Figure 3E-F), particularly in motor sensory
173 regions (white and gray arrowheads in Figure 3E). Due to reduced vessel length density, the
174 overall pericyte cell body coverage (capillary pericyte number per vascular length) is increased
175 by about 10% in sensorimotor areas in aged mice compared to young adult mice (Figure 3G). In
176 contrast to sensorimotor areas, relatively little or even reduced pericyte density and coverage was
177 observed in medial prefrontal areas (Figure 3E white arrow, 3F-G), suggesting regionally distinct
178 vulnerabilities of pericytes with aging.
179 We then asked whether there are selective changes across cortical layers. We noted that
180 the deep cortical layer (L6) showed a selective reduction of pericyte density in the infralimbic
181 cortex, while the superficial layers (2/3 and 4) in the whisker representation of the primary
182 somatosensory cortex ('barrel field') showed a significant increase in the 18-month-old brain
183 compared to the 2-month-old brain (Figure 3H-J). When layer specific density from all
184 isocortical areas was combined, pericyte density was significantly reduced in deep layer 6b in the
185 aged brain, while layers 2/3 and 4 showed significant increases (Figures 3K). Considering layer
186 6b plays a role in brain state modulation [45] and the protective role of pericytes in vascular
187 integrity, significant reduction of the pericytes could make layer 6b and nearby white matter
188 tracks more vulnerable upon aging [37,46].
189
190 **Artery specific labeling shows striking vascular remodeling in penetrating cortical**
191 **arterioles of aged brains.**
192 Previous studies have identified age-related changes in arteries and arterioles in both rodents and
193 humans [47,48]. To investigate potential remodeling in main arteries and penetrating cortical
194 arterioles, we utilized tissue clearing, 3D immunolabeling, and high-resolution light sheet
195 fluorescence microscopy (LSFM) imaging (Figure 4A) (see Methods for more details). We

196 labeled arteries with smooth muscle actin (Acta 2) and transgelin (Sm22) antibodies, pan-
197 vasculature with lectin, and pericytes with CD13 and PDGFRβ antibodies in the same brain. This
198 approach enabled us to examine different vascular compartments and mural cell types in the
199 same intact 3D brain (Figure 4B-H). Despite the volume shrinkage due to dehydration-based
200 tissue clearing methods, we confirmed that the overall vascular geometry was maintained by
201 comparing in vivo two-photon and LSFM imaging from the same animal (Supplementary Figure
202 2).
203 We applied the method to 2-month-old and 24-month-old (late aging) C57BL/6 mice to
204 test whether late aging shows structural remodeling of different vascular compartments and
205 progression of capillary pericyte density reduction. We first focused our analysis on the middle
206 cerebral artery and anterior communicating artery branches contributing to the anterior
207 circulation of the circle of Willis, which is responsible for supplying the majority of cerebral
208 blood flow (Figure 5A). We quantified the average radius of each artery. We did not find
209 significant differences in young and aged mice, nor differences between sexes (Figure 5B-C),
210 suggesting that aging does not impact the diameters of the main arteries of the anterior brain
211 circulation.
212 Next, we examined the number of cortical penetrating arterioles, which are bottlenecks in
213 the supply of blood to the brain [49,50]. There were no significant changes in cortical arteriole
214 numbers (both total arterioles and arterioles that extend into layer 6/corpus callosum) in aged
215 brains compared to the young adult mice (Figure 5D). However, we observed highly tortuous
216 (twisted) vessels across the entire cortex (Figure 5E; highlighted with red arrowheads), which is
217 consistent with prior observations in aged animals and humans [51,52]. Further analysis revealed
218 that aged animals demonstrate increased arteriole tortuosity, as measured by the arc chord ratio
219 (Figure 5F) (see Methods for more details). The number of branching points per arteriole
220 remains similar across the age group (Figure 5G). This increased tortuosity of penetrating
221 arterioles will result in increased blood flow resistance, leading to slowed blood flow with
222 decreased oxygen and nutrient delivery if there is no increase in blood pressure. This decreased
223 flow could make the deep cortical layers and nearby white matter tracks vulnerable during aging
224 [37]. Lastly, we performed vascular tracing using pan-vascular lectin labeling and found no
225 significant difference of vascular length density in the isocortex except a significant reduction in
226 the infralimbic cortex in the 24-month-old mice (Supplementary Figure 3). Moreover, we found
227 that only the cortical layer 6 shows a significant reduction in the vascular length density in the
228 24-month-old mice (Supplementary Figure 3), similar to changes identified in the 18-month-old
229 mice (Figure 2N).
230
231 **Advanced aging is associated with selective loss of capillary pericytes and blood brain**
232 **barrier impairment.**
233 Different pericyte subtypes associate with different vascular branches (Figure 5H) [13]. Aging has
234 been shown to impair specific pericyte subtypes, such as first order (ensheathing) pericytes at the
235 junction between arterioles and microvessels [53]. To examine how different pericyte subtypes are
236 differentially impacted in advanced aging, we used a combination of artery, pan-vascular, and
237 mural cell immunolabeling to distinguish pericyte subtypes at different vascular zones with
238 submicron resolution (0.4 x 0.4 x 1 μm^3) using LSFM imaging (Figure 5I). We successfully
239 visualized individual pericytes and their subtypes, including capillary pericytes, both mesh and
240 thin-strand morphologies, and ensheathing pericytes, which are located along pre-capillary
241 arterioles and express smooth muscle markers such as Acta2 [36] (Figure 5H-I). Examples of

242 different pericyte subtypes (i.e., ensheathing, mesh, and thin strand) are labeled in Figure 5I with
243 cyan, yellow, and purple arrows in each panel, respectively. By following individual vasculature,
244 each pericyte type was manually counted in a region of interest.
245 Consistent with our STPT data, we did not observe any significant changes in pericyte
246 subtype density within the primary somatosensory cortex except a significant reduction of
247 capillary pericyte density in layer 6 (Figure 5J-L). This result further confirmed that pericyte
248 density remains largely unchanged in cortical areas, including contractile ensheathing pericytes.
249 We further examined the entorhinal cortex, since this region is important for memory and is
250 known to be very sensitive to age-related diseases [4,19,38,54–56]. While this region did not show any
251 statistically significant decreases at 18 months of age (early aging) in STPT pericyte mapping
252 (Figure 3B), we found that both mesh and thin-strand pericytes, but not ensheathing pericytes,
253 showed significant reductions in 24-month-old (late aging) mice (Supplementary Figure 4). This
254 suggests that capillary pericytes are at higher risk of cellular density loss, particularly in
255 advanced age.
256 Since pericytes play a key role in regulating blood-brain barrier (BBB) properties [16,46], we
257 examined whether aged brains show leaky BBB properties with compromised tight junction
258 proteins. We analyzed serum protein extravasation in the somatosensory cortex (SS) [57]and found
259 a significant increase in immunoglobulin extravasation throughout the entire layers of the SS
260 (Figure 5M-N), in agreement with an in vivo study [58]. However, we did not find significant
261 changes in the ZO-1 expression, a tight junction marker, in the SS of the aged brain
262 (Supplementary Figure 5). This suggests that the pericyte function to maintain barrier properties
263 is selectively compromised upon aging even without loss of their regional density.
264
265 ***In vivo* imaging to examine hemodynamic changes in aged brains.**
266 In addition to structural changes, the cerebrovasculature may undergo functional changes in
267 neurovascular coupling with aging. Thus, we investigated how normal aging impacts brain
268 hemodynamics during rest and in response to voluntary locomotion and sensory stimulation in
269 awake behaving mice, using wide field intrinsic optical imaging of spectroscopy (IOS) [59] and two-
270 photon laser scanning microscopy (2PLSM) [60–62](Figure 6 and 7). All experiments were performed
271 in awake mice that were head-fixed on a spherical treadmill for voluntary locomotion [59–63].
272 Imaging was performed through polished and reinforced thin-skull windows (PoRTS) to minimize
273 the disruption of the intracranial environment [64]. We utilized two different models, voluntary
274 locomotion [59,61] and whisker stimulation [60,62,65], to quantify the evoked responses. We focused our
275 analysis on two functionally distinct cortical regions, the forelimb/hindlimb representation of the
276 somatosensory cortex (FL/HL) and a frontal cortical region (FC) including the anterior lateral
277 motor cortex (ALM). We targeted ALM because it is involved in motor planning and performs
278 "higher-order" cognitive functions in mice, which makes it analogous to the human prefrontal
279 cortex. We performed these measurements in mice of ages of 2-4 month and 18 month.
280
281 **Neurovascular coupling remains intact in 18-month-old mouse brains.**
282 We first assessed the spatial extent of cortical hemodynamic responses and their relationship to
283 voluntary locomotion, using intrinsic optical signal imaging at multiple wavelengths [59]. Taking
284 advantage of differences in the optical absorption spectra of oxyhemoglobin (HbO) and
285 deoxyhemoglobin (HbR) [66,67], we collected reflectance images during rapid alternating green (530
286 nm) and blue (470 nm) illumination (Figure 6A). When the brain is illuminated with light of
287 different wavelengths, increases in total hemoglobin concentration (ΔHbT) in turn report dilations

288 of arteries, capillaries, and veins, which correspond with increases in cerebral blood volume (CBV).
289 The ΔHbT observed with IOS closely tracks measurements of vessel diameter made with two-
290 photon microscopy [68]. The consistency of microscopic measurements of vessel diameter,
291 combined with its very high signal-to-noise ratio [60], and spatial resolution (less than 200 μm) [69],
292 makes IOS suitable for detecting hemodynamic responses to locomotion. While neurally-evoked
293 dilations initiate in the deeper layers of the cortex, the dilations propagate up the vascular tree to
294 the surface arteries [70–73], where they can be easily detected with IOS.
295 We quantified how locomotion affected CBV in two complementary ways. We calculated
296 the locomotion-triggered average, generated by aligning the IOS or vessel diameter signals to the
297 onset or offset of locomotion using only locomotion events ≥ 5 seconds in duration (Figure 6B and
298 C). Using changes in ΔHbT as an indicator of CBV, we observed region-specific changes in ΔHbT
299 during locomotion (Figure 6B and C). In young adult mice (2-4 months old), there was a
300 pronounced increase in the ΔHbT (corresponding to an increase in CBV) in the forelimb/hindlimb
301 representation of the somatosensory cortex (FL/HL), while in the frontal cortex (FC) there was no
302 change, or even a slight decrease in ΔHbT (n = 7 mice) (Figure 6B and C), consistent with previous
303 reports [59,63,74]. This pattern was not significantly affected by aging, as we observed similar results
304 in 18-month-old (n = 5 mice) (Figure 6B and C).
305 We also calculated the hemodynamic response function (HRF) [60,75], which is the linear
306 kernel relating locomotion events to observed changes in CBV and vessel diameter (Figure 6D
307 and F; see Methods), using all locomotion events. Hemodynamic response functions are used in
308 all of fMRI analyses to extrapolate neuronal activity from a stimulus or a task from hemodynamic
309 signals, and take into account the slower responses of the vasculature relative to neurons [76]. Using
310 the HRFs to quantify the net CBV, we obtained the same conclusions as derived from the
311 locomotion-triggered average, i.e., the net increase in cerebral blood volume does not change
312 significantly during aging (Figure 6E and G, left) in either FC or FL/HL (2-month: 0.53 ± 0.18
313 μM; 18-month: 0.57 ± 0.06 μM). In addition to the amplitude of the hyperemic response evoked
314 by locomotion, HRFs also provide us information regarding the temporal dynamics of CBV
315 responses. We found that the onset time (Figure 6E, middle, 2-month: 0.95 ± 0.15 s; 18-month:
316 0.95 ± 0.14 s) and duration (Figure 6E, right, 2-month: 1.11 ± 0.12 s; 18-month: 1.24 ± 0.24 s) of
317 locomotion evoked hyperemic response remained similar in aged brains. To further validate the
318 results from HRFs, we quantified the responses of ΔHbT in response to brief whisker stimulation
319 (100 ms duration) (Figure 6H). We observed that in response to contralateral whisker stimulation,
320 the ΔHbT response remains similar in 18-month-old brains compared to 2-month-old brains
321 (Figure 6I-L).
322 In addition to the mesoscopic level measurements using IOS, we further compared whether
323 hemodynamics was different between age groups at individual vessel level in FL/HL, in terms of
324 pial arterial diameter change in response to locomotion, using *in vivo* 2PLSM (Figure 6M). The
325 locomotion-evoked arterial diameter change (Figure 6N), as well as the HRF of arterial diameter
326 change (Figure 6O) showed a similar spatial pattern of responses as the CBV measured using IOS,
327 despite a trend of delayed response during aging.
328 Finally, to determine whether vascular dilation capacity was intact in aged mice, we
329 measured the mesoscopic brain hemodynamic responses using IOS (Figure 6P) and microscopic
330 vessel diameter response to isoflurane, a potent vasodilator, using 2PLSM. In FL/HL, we observed
331 an increase of ΔHbT (2-month: 176.8 ± 29.5 μM, 4 mice; 18-month: 146.7 ± 22.2 μM, 4 mice)
332 and arteriole diameter (2-month: 65.5 ± 19.2%, 4 mice; 18-month: 51.7 ± 10.8%, 5 mice;data not
333 shown) under isoflurane. In FC, we observed an increase of ΔHbT (2-month: 106.6 ± 28.5 μM, 4

334 mice; 18-month: 85.4 ± 23.0 μM, 4 mice). The extent of vasodilation observed between young and
335 old mice was not different when animals were transitioned from air to 5% isoflurane, suggesting
336 the dilation capacity remains similar across different age groups.
337
338 **Oxygenation carrying capacity is decreased in aged mice.**
339 One of the important functions of increased blood flow/volume is to deliver oxygen to the brain.
340 Using the cerebral oxygenation index (HbO-HbR) [59,77], a spectroscopic measurement of
341 hemoglobin oxygenation, we saw an increase in oxygenation during locomotion in both FC and
342 FL/HL areas in young mice. The oxygen increase in response to locomotion (Figure 7A) did not
343 significantly differ across age groups. As vasodilation is one of the determining factors controlling
344 brain oxygenation [59], we quantified the relationship between locomotion-evoked responses of
345 ΔHbT and ΔHbO-HbR using linear regression. The slope and intercept of the fitting decreased
346 with the healthy aging process (2-month: $y = 0.8667x + 35.43$; 18-month: $y = 0.5209x + 27.37$;
347 Figure 7B), which suggests that oxygen carrying capacity for the red blood cells decreases during
348 aging, and that the aging brain has lower baseline oxygenation, respectively.
349 To determine whether the oxygen exchange and oxygen delivery capacity were intact in
350 aged mice, we measured the brain tissue oxygenation response when mice breathed 100% oxygen
351 (Figure 7C-F). We observed that the oxygen delivered to the brain is significantly smaller in the
352 aged mouse brain, both in the FC (2-month: 43.7 ± 4.1 μM; 18-month: 32.5 ± 10.4 μM. Linear
353 mixed effects model, $p = 0.0536$) and FL/HL (2-month: 71.0 ± 14.4 μM; 18-month: 51.0 ± 5.3 μM.
354 Linear mixed effects model, $p = 0.0097$).
355 Lastly, we quantified the functions of the brain capillary network during aging progress, as
356 its dynamics affect brain oxygenation responses [59,78]. We first compared whether red blood cell
357 (RBC) velocity differed between age groups in the capillary network. We found no significant
358 differences in lumen diameter between different groups (2-month: 4.7 ± 1.65 μm, 32 capillaries;
359 18-month: 4.9 ± 1.2 μm, 36 capillaries), a trend toward decreased RBC velocity, but not a
360 statistically significant difference (2-month: 0.58 ± 0.33 mm/s; 18-month: 0.53 ± 0.34 mm/s)
361 (Supplementary Figure 6A), no difference in hematocrit (2-month: 38.3 ± 7.6%; 18-month: 33.4
362 ± 9.6%; Supplementary Figure 6B). In addition to RBC flow rate and hematocrit, the "stochastic"
363 nature of red blood cell distribution in the capillary also affects brain oxygenation [61,78]. When we
364 quantified the spacing of RBC and the occurrence of "stall" events, we found no significant
365 difference between different aging groups (Supplementary Text 1).
366 Collectively, our *in vivo* recording results suggest relatively intact vascular response
367 dynamics and decreased oxygen-carrying capacity in 18-months-old mice (early aging), which
368 can create imbalances in baseline and on-demand supply of oxygen in aged brains.
369
370
371
372

Discussion

Understanding structural and functional changes of the cerebrovasculature during normal aging will provide foundational information to understand altered brain energy infrastructure that can be commonly linked with many neurodegenerative disorders. Here, we provide detailed information regarding anatomical changes of the cerebrovascular network and physiological alteration of the blood flow in aged mouse brains, as summarized in Figure 8. We found overall reductions in vascular length and branching densities with BBB impairment, along with more tortuous arterioles that indicate sparser and remodeled vascular networks in aged brains. We also uncovered selective vascular and pericyte loss in cortical deep layers, basal forebrain regions, and the hippocampal network, including the entorhinal cortex, which may contribute to their regional vulnerabilities in neurodegenerative disorders [44,79]. Lastly, our *in vivo* studies showed inefficient oxygen delivery in aged brains despite relatively intact neurovascular coupling response time. Collectively, our results advance our understanding of global changes and regional vulnerabilities associated with deteriorating vascular networks in aged brains.

Cerebrovascular structural changes with selective pericyte reduction in aged brains.

Previous studies in aged cerebral vasculature have shown stiffened arteries, microvascular rarefaction, and remodeled vascular trees in selected brain regions [17,20,80–82]. Our study showed that there is an approximate 10% decrease in overall vascular density, as well as branching density, in 18-month-old compared to 2-month-old mouse brains, suggesting a sparser vascular network to distribute the blood [35]. Moreover, aged brains showed substantially more tortuous penetrating arterioles, which impede blood flow by increasing flow resistance. This increase in resistance, unless countered by an increase in blood pressure, could result in reduced oxygen and nutrient supply, particularly areas distal to main arteries such as the deep cortical layers and white matter tracks [20,37,83]. Importantly, both human and murine studies have shown similar changes with tortuous vasculature, decreased vascular density, and associated slowed cerebral blood flow [20,22,81,84,85]. Such changes can lead to an increased heart rate to compensate for cerebral hypoperfusion, as frequently observed in elderly population [86]. We also found an overall increase in average vessel radii, which is largely contributed to by the microvasculature. Notably, pericytes are known to regulate the basal tone and permeability of microvessels, and release neurotropic factors [13,15,16,46]. A recent study also showed that pericytes in superficial cortical layers have impaired recovery of cellular processes in the aged brain [36]. Furthermore, we found that aged brains have a compromised BBB with increased immunoglobulin extravasation throughout cortical layers in aged brains [58]. Therefore, while pericyte cell density does not change significantly during aging, their regulatory function may be impaired, resulting in slightly dilated and leaky cerebrovasculature.

Our data showed that the vasculature of the isocortex is more resilient to aging compared to other brain regions, as evidenced by no significant changes in both microvascular and capillary pericyte densities. However, deep cortical layers, especially layer 6b, showed reduced vessel density and pericyte density, consistent with previous studies [87]. Notably, layer 6 plays a crucially important role as the output layer to the thalamus [45,88]. Moreover, layer 6b is the only cortical layer that is responsive to sleep-wake neuropeptides such as orexin, which is produced in the lateral hypothalamus [88,89]. Considering that sleep is often dysregulated with increased age in humans [90], failing cerebrovascular network in the deep cortical layer may provide important insight to understand aging related sleep dysregulation.

419 Since our 3D mapping data examine vascular network changes of the whole mouse brain
420 in an unbiased way, we identified specific brain regions with selective vulnerabilities in aged
421 brains. For example, we found significantly reduced vascular and pericyte densities in the basal
422 forebrain area, which contains cholinergic neurons [91]. The basal forebrain cholinergic neurons
423 (BFCNs) have highly extensive projections to the cortical area and have large soma size with
424 high energy demands [92]. Previous clinical and preclinical studies have shown that BFCNs are
425 highly vulnerable in Alzheimer's disease (AD) and their deterioration is linked with memory
426 impairment [44,93]. Impaired vascular networks with decreased pericyte density may, potentially
427 serve as an underlying cause of BFCN degeneration in normal aging and neurodegenerative
428 disorders, including AD [79,94,95]. Another notable area is the entorhinal cortex (ENT), a part of the
429 hippocampal network, which has been heavily implicated in AD and particular cognitive deficits
430 [96,97]. The lateral ENT (ENTl) in aged brains showed significantly decreased vascular length,
431 branching point, and capillary pericyte density, consistent with *in vivo* ultrasound
432 measurement[82]. The ENTl vascular density is one of lowest across the brain region in normal
433 adult mice [29]. This indicates that the entorhinal cortex is likely to be particularly susceptible to
434 further insult (e.g., hypoxia), which may explain its vulnerability in neurodegenerative disorders.
435 Lastly, our study identified specific thalamic and hypothalamic areas with decreases in the
436 vascular network density, such as the medial preoptic area. This is particularly striking as the
437 thalamus has recently been identified as a region vulnerable to microbleeds in aged mice [98]. This
438 warrant future studies for these largely understudied subcortical areas in aging research.
439
440 **Inefficient oxygen delivery in aged brains.**
441 We found that brain hemodynamic responses including the increase in blood flow during
442 locomotion and whisker stimulation in 18-month-old mice remained relatively intact. This
443 suggests that the aged brain can still deliver enough red blood cells to the regions with energy
444 demands. In contrast, the baseline oxygenation and oxygen carrying capacity of the red blood
445 cells decrease with age. Notably, respiration is an important regulator of brain oxygenation [59],
446 and lung function decreases during the aging process [99,100]. The decreased ability to deliver
447 oxygen can also be related to decreased microvessel density and its connectivity, resulting in less
448 effective oxygen distribution, and the shift of the oxyhemoglobin dissociation curve with age [101].
449 This baseline drop in brain oxygenation will make the brain more vulnerable to hypoxia when
450 facing increased oxygen demand, as neurons become hyperexcitable in aged brains [102–104]. In
451 addition, aged mice have impaired hypoxia-induced vessel formation, which is a known
452 compensatory mechanism [105]. This baseline drop in brain oxygenation, paired with reduced
453 vascular density, reduced vascular plasticity as well as increased blood flow resistance due to
454 increased vessel tortuosity, will make brain areas in distal vascular territories, such as white
455 matter tracks, and watershed areas (located at the junction between main artery territories)
456 selectively vulnerable in aged brains [22,106]. Indeed, recent studies have demonstrated *in vivo* that
457 aged animals, beginning at 18 months of age and becoming prominent at 24 months, have
458 decreases in CBF correlated with areas of increased tortuosity in cortical areas [20,82].
459 We also found significant reductions in vascular and pericyte densities within the deepest
460 cortical layers, particularly layer 6b that are likely related to the blood flow responses in both
461 deep and superficial layers of the aged mouse cortex. A recent study utilizing 3-photon *in vivo*
462 imaging demonstrated reduced vascular density with vascular network simplification and
463 increased flow resistance in layer 6 and the corpus callosum of the somatosensory cortex, while

there are increases in baseline RBC flow velocity and flux in the superficial layer [37]. In parallel, our *in vivo* measurement for evoked neurovascular coupling (Fig. 6 and 7) showed that functional hyperemia in the superficial layer is largely intact while RBC oxygen-carrying capacity is significantly reduced. Collectively, this evidence suggests that the detrimental effects of aging occur most significantly in the deep cortical layer and may trigger potential compensatory response (e.g., increased density of pericytes) in the superficial layer, which can lead to a redistribution of blood flow toward the superficial cortical layer [37]. Coupled with less efficient on-demand oxygen delivery, these age-related changes will make deep cortical layers highly vulnerable. There is evidence that exercise can help ameliorate age-related declines in perfusion and oxygenation [107].

Limitations of the Study

In our anatomical studies, we found significant vascular loss in deep cortical areas and many subcortical areas (e.g., basal forebrains, hypothalamus, and entorhinal cortex). However, our *in vivo* measurement is limited to superficial cortical layers, where we did not observe dramatic anatomical changes. Although the brain hemodynamics at the surface reflect the dynamics along the vascular tree, future studies with emerging techniques such as functional ultrasound imaging or three-photon microscopy imaging will help to address functional changes in these important, yet hard-to-reach brain areas [108,109]. Another potential limitation to this work is that most C57Bl/6 aged animal groups were obtained directly from commercial vendors which could confer differences in housing, nutrition, shipping, and handling compared to the young adult mice raised in-house. While this is unlikely to overshadow the differences due to aging, these factors could potentially impact the vasculature. Moreover, our analysis mostly focuses on the arterial and capillary compartments of the vasculature. Future studies are needed to elucidate how aging affects the structure and function of the venous side of aged brains.

Summary

Taken together, our study reveals aging-related brain-wide and area-specific changes in vascular and mural cell types. These changes can explain the vulnerability and resilience of different brain areas in normal aging. Moreover, we identified an age-related decrease in brain oxygenation and delayed neurovascular coupling, which can be linked with cognitive impairment in aged brains. These aging-related changes will serve as a common factor in understanding many neurodegenerative disorders and cognition decline in the elderly population.

Acknowledgments
We thank Josephine Liwang for constructive discussion of the manuscript, Dr. Volkhard Linder for kindly sharing PDGFRβ-Cre transgenic mice and Dr. Zhuhao Wu for sharing tissue clearing protocol. We thank Jen Minteer and Becca Betty for valuable management of our animal colony, as well as the coding support provided by Fae Kronman. We acknowledge the use of computational resources in the High Performance Computing cluster at the Penn State College of Medicine.
Funding:
National Institutes of Health grant R01NS108407 and RF1MH12460501 (YK)
National Institutes of Health grant R01NS078168 and R01NS101353 (PJD)
American Heart Association Career Development Award #935961 (QZ)
Its contents are solely the responsibility of the authors and do not necessarily represent the views of the funding agency.

Author Contributions
Conceptualization: YK, HCB
Anatomical Data Collection: HCB, QZ, SB, UC, YK
Developing Computational Analysis: YTW, DJV
Data Analysis: HCB, QZ, YTW, SB, DJV, DS, HP, YK
In vivo Imaging and related analysis: QZ, PJD
Manuscript preparation: HCB, YK, QZ, SB with help from other authors.

Inclusion and ethics statement
All collaborators of this study who met the authorship criteria mandated by Nature Portfolio journals have been recognized as authors, as their involvement and contributions were crucial for study implementation. Collaborators agreed upon their respective roles and responsibilities ahead of the research.

Declaration of Interests
The authors declare no competing interests.

RESOURCE AVAILABILITY

Lead contact

Further information and requests for resources should be directed to and will be fulfilled by the lead contact, Yongsoo Kim (yuk17@psu.edu).

Materials availability

This study did not generate new unique reagents.

Code availability

All available codes are deposited in a public data repository (https://github.com/yongsookimlab).
Custom code for serial two photon tomography image stitching is available at
https://github.com/KimLabResearch/TracibleTissueCyteStitching
Deep learning network based pericyte detection code at
https://github.com/yongsookimlab/Multi_resolution_DLNN_Cell_Counting
Light sheet fluorescence microscopy imaging stitching algorithms at
https://github.com/yongsookimlab/LSFM_Image_Stitcher
Vascular tracing algorithm at https://github.com/yongsookimlab/MiceBrainVasculatureTracer
Cortical flatmap at https://github.com/KimLabResearch/CorticalFlatMap
All codes can be used without restriction.

Data availability

All datasets can be used for non-profit research without any restriction. Any additional information required to reanalyze the data reported in this paper is available from the lead contact upon request.

565 **METHODs**
566
567 **Animals**
568 Animal experiments were approved by the Institutional Animal Care and Use Committee at Penn
569 State University. Adult male and female mice were used across all age and genotype groups in
570 this study.
571 For transgenic pericyte-specific experiments, PDGFRβ-Cre mice (a kind gift from the
572 Volkhard Lindner Lab) [40] were crossed with female Ai14 mice which express a Cre-dependent
573 tdTomato fluorescent reporter (LoxP-Stop-LoxP-tdTomato). These PDGFRβ-Cre:Ai14 mice
574 exhibit PDGFRβ expression in two distinct mural cell types, pericytes and vascular smooth
575 muscle cells. Both the adult 2-month-old and 18-month-old PDGFRβ-Cre:Ai14 mice were bred
576 and aged in house. We used tail genomic DNA with PCR for the transgenic mouse lines
577 requiring genotyping. Adult 2-month-old C57BL/6J mice were bred from C57BL/6J mice
578 directly obtained from the Jackson Laboratory and used for vascular tracing experiments with
579 FITC filling (n=4) [29]. 18-month-old C57BL/6J mice utilized for FITC-fill vascular mapping
580 experiments were obtained directly from Jackson and Charles River laboratories. 24-month-old
581 C57BL/6J mice used for the current study were directly obtained from the National Institute of
582 Aging at 18 months and aged to 24 months in house. All animals were used once to generate
583 data, and aged animals with tumors or other appreciable abnormalities were excluded from
584 analysis.
585 For the *in vivo* two-photon imaging experiments, a total of 24 C57BL/6J mice of both sexes
586 (2-18 months old, 18-35 g, Jackson Laboratory) were used. Recordings of cerebral blood volume
587 and cerebral oxygenation response to locomotion were made from 12 mice (2-4 month old: n = 7
588 mice; 18-month-old: n = 5 mice) using wide field optical imaging. In a subset of the young mice
589 (2-4 month old: n = 5 mice) and an additional set of aged mice (18 month old: n = 4 mice), we also
590 recorded cerebral blood volume and cerebral oxygenation response to whisker stimulus using
591 optical imaging. Recordings of stacks, capillary blood flow velocity, and diameters of arteries and
592 veins using two-photon laser scanning microscopy (2PLSM) were conducted in 15 mice (12 of
593 these 15 mice were also used for wide field optical imaging; 2-4 month old: n = 10 mice; 18-month
594 -old: n = 5 mice). Mice were given food and water *ad libitum* and maintained on 12-hour (7:00–
595 19:00) light/dark cycles. All experiments were conducted during the light period of the cycle.
596
597 **Perfusion based vascular labeling, STPT imaging, and computational analysis**
598 Overall procedure remains similar to our previous publication [29]. The detailed procedure has
599 been included in a separate protocol paper [33]. Briefly, animals were deeply anesthetized with
600 ketamine-xylazine, and perfused with 1X PBS followed by 4% paraformaldehyde to wash out
601 blood and allow for tissue fixation, respectively. For vessel labeling, immediately following 4%
602 paraformaldehyde, 0.1% (w/v) fluorescein isothiocyanate (FITC)-conjugated albumin (Sigma-
603 Aldrich, cat.no.: A9771-1G) in a 2% (w/v) solution of porcine skin gelatin (Sigma-Aldrich,
604 cat.no: G1890-500G) was perfused to obtain vascular filling. For STPT imaging, the brain
605 sample was embedded in oxidized agarose and cross-linked in 0.05M sodium borohydrate at 4°C
606 for at least 2 days ahead of imaging. We used 910nm wavelength (UltraII, Coherent) as
607 excitation light for all samples. Signals in the green and red spectrum were simultaneously
608 collected using 560 nm dichroic mirror at x,y = 1,1 μm resolution in every 50 μm z (for pericyte
609 mapping) or x,y,z = 1,1,5 μm resolution (for vascular mapping).

610 We utilized our previously described software pipeline to perform de-aberration,
611 normalization, and imaging stitching steps for all STPT data collected for this study [29].
612 Moreover, we used the same analytical tools to binarize the vessel signals and skeletonize for
613 further analysis. This pipeline also performs cleaning/reconnecting of artifacts, traces the vessel
614 diameter, and finally outputs the coordinates for each vessel segment and its connectivity. The
615 distance to the nearest vasculature is calculated by probing all tissue space in the data and finding
616 the average distance to its nearest vasculature surface. For every point being probed, we first take
617 all the vasculature data within the +/- 100 µm cartesian coordinated cube and calculate the
618 straight-line distance between the probe and each vascular data point inside the cube. Then we
619 take the minimum of those distances as the distance to the nearest vasculature for that probing
620 point. We performed our calculation at 10 µm isotropic voxel resolution probing, which provides
621 enough data entry for each ROI that is at least 100 µm in size. For pericyte cell counting, we
622 used previously developed Deep Learning Neural Network (DLNN) cell counting [29]. This DLNN
623 uses a per-cell multi-resolution-hybrid ResNet classification with potential cell locations to
624 reduce computational time and resources without loss of quality. While aged mouse brains do
625 have increased noise due to the accumulation of cellular debris, we validated that our DLNN
626 pipeline performed at the same level as with young adult mice and did not incorporate cellular
627 debris as potential cells.
628
629 **Tissue clearing, 3D immunolabeling, and LSFM imaging**
630 Whole brain vascular staining was performed following the iDISCO+ protocol with
631 modifications [25]. Brain samples were delipidated in SBiP buffer, consisting of ice-cold water,
632 50mM Na_2HPO_4, 4% SDS, 2-methyl-2-butanol and 2-propanol. This buffer is activated at room
633 temperature and is therefore made and stored at 4°C before use. Each sample was submerged in
634 10ml of SBiP buffer, rotated at room temperature with buffer changes at 3 hours, 6 hours and
635 then incubated with fresh SBiP buffer overnight. For adequate delipidation, particularly for aged
636 samples, each brain was then washed with SBiP for a total of 6 days, with daily buffer changes.
637 After delipidation, brain samples were washed with B1n buffer, which consists of 0.1% TritonX-
638 100, 1g of glycine, 0.01% 10N NaOH and 20% NaN3. Brain samples were washed with 10ml of
639 B1n buffer at room temperature for 2 days. To begin immunolabeling, brains were rinsed 3 times
640 for 1 hour each with PTwH buffer, consisting of 1X PBS, 0.2% Tween-20, 10mg heparin, and 2g
641 of NaN3. For primary antibody incubations, antibodies were diluted in antibody solution
642 consisting of PTwH buffer with 5% DMSO and 3% normal donkey serum. Antibodies to smooth
643 muscle actin (Acta2) (Rabbit anti-Acta2, Abcam, cat: ab5694, dilution 1:1000) and transgelin
644 (Sm22) (Rabbit anti-Sm22 Abcam, cat: ab14106, dilution 1:1500) were combined to label the
645 artery wall, as previously described [25]. Pan-vascular labeling was achieved through staining with
646 DyLight-594 labeled Lycopersicon Esculentum (Tomato) Lectin (Vector labs, cat. no.: DL-1177-
647 1), which was added to both primary and secondary incubations at 1:100 concentration. Pericytes
648 were labeled by combining PDGFRβ (Goat anti- PDGFRβ, R&D Systems, cat. no.: AF1042,
649 dilution: 1:100) and Mouse Aminopeptidase N/CD13 (Goat anti-CD13, R&D Systems, cat. no.:
650 AF2335, dilution: 1:100). Primary antibodies were incubated for 10 days at 37°C. Following
651 primary incubation, PTwH buffer was changed 4-5 times for each sample over the course of 24
652 hours. A fresh antibody solution was used to dilute all secondary antibodies to a concentration of
653 1:500. For secondary antibodies, Alexa Fluor® 488-AffiniPure Fab Fragment Donkey Anti-
654 Rabbit IgG (H+L) (Jackson ImmunoResearch laboratories, cat. no.: 711-547-003) was used to
655 detect artery staining and Alexa Fluor® 647-AffiniPure Fab Fragment Donkey Anti-Goat IgG

656 (H+L) (Jackson ImmunoResearch laboratories, cat. no.: 705-607-003) was utilized to detect
657 pericyte staining. After secondary incubation for 10 days at 37°C, brains were washed 4-5 times
658 in PTwH buffer for 24 hours. Brain samples were then dehydrated in a series of methanol
659 dilutions in water (1-hour washes in 20%, 40%, 60%, 80% and 100%). An additional wash of
660 100% methanol was conducted overnight to remove any remaining water. The next day, brains
661 were incubated in 66% dichloromethane/33% methanol for 3 hours and subsequently incubated
662 in 100% dichloromethane twice for at least 15 minutes each. Brains were equilibrated in
663 dibenzyl ether for at least two days before transitioning to ethyl cinnamate one day prior to
664 imaging.
665 We used the SmartSPIM light sheet fluorescence microscope (LifeCanvas Technologies).
666 Brains were supported in the custom sample holder by standardized pieces of dehydrated agarose
667 consisting of 1% agarose in 1X TAE buffer. The sample holder arm was then submerged in ethyl
668 cinnamate for imaging. We used a 3.6X objective (LifeCanvas, 0.2NA, 12mm working distance,
669 1.8µm lateral resolution) and three lasers (488nm, 560nm, 642nm wavelengths) with a 2mm step
670 size. For detailed examination of pericytes, we used a 15X objective (Applied Scientific
671 Instrumentation, 0.4NA, 12mm working distance, 0.4mm lateral resolution) with a 1µm z step
672 size. Acquired data was stitched using custom Matlab codes adapted from Wobbly Stitcher [25].
673
674 **Analysis of LSFM-based vascular and pericyte signals**
675 For pericyte counting, prior to quantification, each stitched image stack, per signal channel, was
676 separately normalized, and the entire volume of each image stack was then converted to 20 µm
677 maximum intensity projections (MIP). Normalization of each signal channel is done by adjusting
678 according to the histogram-determined global mean value of the background by utilizing a 10x
679 downsized copy of the entire image stack. The 20µm MIP step was determined to prevent over or
680 under counting of cell bodies, since pericyte cell body size tended to range from 6-10µm
681 depending on the orientation of the cell measured within a 3D context in the original image
682 stack. Finally, all three image channels (artery, lectin, and mural cell labels) were merged into a
683 channel overlay to provide additional context, such as vascular zone information. Cells with
684 stereotypical pericyte morphology (i.e., ovoid shape and protruding from the vessel wall),
685 typically along the first through third order arteriolar branches, that also expressed smooth
686 muscle markers and extended processes that wrapped around the vessel were classified as
687 ensheathing pericytes. Capillary pericytes were classified according to cell body shape and
688 localized to the capillary bed without any Acta2/Transgelin expression. These cells were further
689 subdivided into mesh or thin strand morphologies according to their microvessel placement and
690 type of processes, according to the definitions of these subtypes [110]. Cell bodies along larger
691 veins, including the principal cortical venules were excluded from this analysis.
692 For arteriole analysis, 600 µm MIPs were obtained from the channel labeling of Acta2
693 and Transgelin (i.e., artery labeling). We cropped the supplementary somatosensory cortex from
694 full datasets and quantified the total number of arteries and their branches manually.
695 For tortuosity measurements, a centerline of the entire vessel length was first traced to
696 obtain the Euclidean distance (arc length) using a skeletonization tool in Clearmap 2.0 [25]. Then a
697 straight line connecting the start and end points of the previous length was obtained to measure
698 the chord length. The arc chord ratio was then determined by dividing the Euclidean distance by
699 the arc chord distance. We used 32 arteries from 2-month-old (n=3 animals) and 23 from 24-
700 month-old (n=3 animals) in the medial prefrontal, and 19 arteries from 2-month-old (n=2
701 animals) and 23 from 24-month-old (n=3 animals). For Circle of Willis analysis, entire brain

datasets for the artery channel were converted to 10µm isotropic. Next, a cropped volume including the branching point of the middle cerebral artery as well as ample segments of the anterior communicating artery and middle cerebral artery were obtained within 250x250x120 µm (x,y,z) to fully capture the entire branch point and associated arteries in x,y,z dimensions. This subset was re-sliced to obtain the cross-sectional area of this section of the vessel. The average radius was obtained from the cross-sectional areas.

For length density measurement, we modified TubeMap vascular tracing codes [25]. We devised an ilastik machine learning-based vascular detection method using all three imaging channels followed by binarization and skeletonization. We used TubeMap graph tracing tool and Elastix based image registration to quantify vascular length and volumes across different brain regions.

To compare the vasculature between *in vivo* two-photon and LSFM imaging from the same brain, we found a matched imaging window based on vascular architecture and overall brain anatomy in both imaging. We conducted vessel diameter measurements in 2D with vasometric (ImageJ) that allows for line measurements of diameter at every 2 µm intervals.

We initially acquired LSFM data with vascular labeling (n = 9 each for 2 months and 24 months old) and used them for Circle of Willis analysis. We used a subset of samples randomly chosen from data with satisfactory immuno-staining qualities of target structures.

Immunohistochemistry

The mice were deeply anesthetized using isoflurane and then decapitated with scissors. The brain was immediately extracted and submerged in optimal cutting temperature medium (Tissue-Tek). Rapid freezing of the immersed brain was achieved by exposure to dry ice-chilled 2-methylbutane. This frozen brain tissue was subsequently stored at −80 °C until needed. Coronal brain sections, each 10 µm thick, were obtained using a cryostat. Once brought to room temperature, the sections were fixed using a 4% paraformaldehyde solution. After fixation, the sections underwent a sequence of steps: they were rinsed three times in 1X PBS and then blocked for an hour at room temperature using 1% donkey serum diluted in PBST (1x PBS+ 0.03% Triton-X). Following blocking, the slices were incubated overnight at 4 °C in a primary antibody solution (polyclonal rabbit anti-zo-1, Invitrogen Cat# 40-2200, RRID:AB_2533456, diluted 1:200) in the blocking buffer with gentle rotation. Post-primary antibody incubation, the slices were washed three times in 1X PBS and then incubated for 1 h at room temperature with a secondary antibody (Donkey anti-rabbit conjugated with Alexa 568, Thermo Fisher Scientific Cat# A10042, RRID:AB_2534017, diluted 1:500) along with DyLight-488 labeled Lycopersicon Esculentum (Tomato) Lectin (Vector Laboratories Cat# DL-1174, RRID:AB_2336404, dilution 1:100). Prior to mounting, the slices were washed three times in 1X PBS and then mounted using vectashield mounting media containing DAPI (Vector Laboratories Cat# H-1500, RRID:AB_2336788).

For IgG staining, the procedure was used for fixing and blocking. Subsequently, the sections were incubated for 20 hours at 4°C with anti-IgG (CF640R, Biotium Cat# 20177, RRID:AB_10853475, dilution 1:100) in blocking buffer. Following this incubation, the samples were washed three times with 1X PBS and incubated with DyLight-488 labeled Lycopersicon Esculentum (Tomato) Lectin (Vector Laboratories Cat# DL-1174, RRID:AB_2336404, dilution 1:100) for 1 h at room temperature. After three washes with 1X PBS, the sections were mounted using vectashield mounting media containing DAPI (Vector Laboratories Cat# H-1500, RRID:AB_2336788).

<u>Images were acquired using a confocal microscope (Zeiss LSM900 with Airyscan 2) using a 20x objective. The images were then binarized and area coverage was calculated using ‘analyze</u>

748 particles' function in ImageJ. All the images for the same staining were imaged under the same
749 settings and were analyzed using the same binarizing parameters.
750
751 **Surgery, habituation, and measurement for *in vivo* recording**
752 Cerebral oxygenation, cerebral blood volume (CBV) and vessel diameter data were acquired from
753 the same groups of awake, behaving mice during voluntary locomotion and whisker stimulation.
754 All surgeries were performed under isoflurane anesthesia (in oxygen, 5% for induction and 1.5-2%
755 for maintenance). A custom-machined titanium head bolt was attached to the skull with
756 cyanoacrylate glue (#32002, Vibra-tite). The head bolt was positioned along the midline and just
757 posterior to the lambda cranial suture. Two self-tapping 3/32" #000 screws (J.I. Morris) were
758 implanted into the skull contralateral to the measurement sites over the frontal lobe and parietal
759 lobe. For measurements using two-photon laser scanning microscopy (2PLSM), CBV
760 measurement using intrinsic optical signal (IOS) imaging or brain oxygenation measurement using
761 spectroscopy, a polished and reinforced thin-skull (PoRTS) window was made covering the right
762 hemisphere or both hemispheres as described previously [59–64,68]. Following the surgery, mice were
763 then returned to their home cage for recovery for at least one week, and then started habituation
764 on experimental apparatus. Habituation sessions were performed 2-4 times per day over the course
765 of one week, with the duration increasing from 5 min to 45 min.
766 Habituation. Animals were gradually acclimated to head-fixation on a spherical treadmill
767 [59,61,63,111] with one degree of freedom over at least three habituation sessions. The spherical
768 treadmill was covered with nonabrasive anti-slip tape (McMaster-Carr) and attached to an optical
769 rotary encoder (#E7PD-720-118, US Digital) to monitor locomotion. Mice were acclimated to
770 head-fixation for ~15 minutes during the first session and were head-fixed for longer durations (>
771 1 hour) in the subsequent sessions. Mice were monitored for any signs of stress during habituation.
772 In all cases, the mice exhibited normal behaviors such as exploratory whisking and occasional
773 grooming after being head-fixed. Heart rate fluctuations were detectable in the intrinsic optical
774 signal [59,68] and varied between 7 and 13 Hz for all mice after habituation, which is comparable to
775 the mean heart rate (~12 Hz) recorded telemetrically from mice in their home cage [112]. Habituation
776 sessions were achieved 2-4 times per day over the course of one week, with the duration increasing
777 from 5 min to 45 min. Mice that received whisker stimulation (n = 9) were acclimatized to head-
778 fixation for 15–30 min during the first session. In subsequent sessions, they began to receive air
779 puffs directed at the whiskers and were head-fixed for longer durations (> 60 minutes).
780 Physiological measurements. Data from all experiments (except two photon laser scanning
781 microscopy) were collected using custom software written in LabVIEW (version 2014, National
782 Instruments). We focused on two different brain areas, the somatosensory cortex (the
783 forelimb/hindlimb area, FL/HL) and a frontal cortical region (FC) including the anterior lateral
784 motor cortex (ALM). The coordinates are as follows: 0-1 mm caudal and 1-2 mm lateral from
785 bregma, ~1 mm^2 for FL/HL and 2–4mm rostral and 0.5–2.5mm lateral from bregma, ~4mm^2 for
786 the ALM.
787 *Behavioral measurement.* The treadmill movements were used to quantify the locomotion
788 events of the mouse. The animal was also monitored using a webcam (Microsoft LifeCam
789 Cinema®) as an additional behavioral measurement.
790 *Vibrissa stimulation*. Animals were awake and engaged in whisking behavior during IOS
791 data acquisition [60,62]. Brief (0.1-s duration) puffs of air were delivered to the ipsilateral and
792 contralateral whiskers through a thin plastic tube (length 130 mm, diameter 2 mm). Air puffs were
793 directed to the distal ends of the whiskers at an angle parallel to the face to prevent stimulation of

794 other parts of the head or face. An additional air puffer was set up to point away from the body for
795 use as an auditory stimulus. The puffs were delivered via solenoid actuator valves (Sizto Tech
796 Corporation, 2V025 1/4) at constant air pressure (10 psi) maintained by an upstream regulator
797 (Wilkerson, R03-02-000). Air puffs were separated by intervals of 30-60 s, and the order of all
798 sensory stimulation was randomized, with a nominal ratio of three contralateral stimuli for every
799 ipsilateral or auditory stimulation. Auditory and ipsilateral stimuli were omitted from the principal
800 analysis because their responses were primarily related to stimulus-provoked movement.
801 *Brain oxygen measurement using optical imaging*. We mapped the spatiotemporal
802 dynamics of oxyhemoglobin and deoxyhemoglobin concentrations using their oxygen-dependent
803 optical absorption spectra [78]. Reflectance images were collected during periods of green LED light
804 illumination at 530 nm (equally absorbed by oxygenated and deoxygenated hemoglobin, M530L3,
805 Thorlabs) or blue LED light illumination at 470 nm (absorbed more by oxygenated than
806 deoxygenated hemoglobin, M470L3, Thorlabs). For these experiments, a CCD camera (Dalsa
807 1M60) was operated at 60 Hz with 4X4 binning (256 X 256 pixels), mounted with a VZM300i
808 optical zoom lens (Edmund Optics). Green and blue reflectance data were converted to changes in
809 oxy- and deoxyhemoglobin concentrations using the modified Beer-Lambert law with Monte
810 Carlo-derived wavelength-dependent path length factors [67]. We used the cerebral oxygenation
811 index [77] (i.e., HbO-HbR) to quantify the change in oxygenation, as calculating the percentage
812 change requires knowledge of the concentration of hemoglobin on a pixel-by-pixel basis, which is
813 not feasible given the wide heterogeneity in the density of the cortical vasculature [32].
814 *Measurements using two-photon laser scanning microscopy (2PLSM)*. Mice were briefly
815 anesthetized with isoflurane (5% in oxygen) and retro-orbitally injected with 50 µL 5%
816 (weight/volume in saline) fluorescein-conjugated dextran (70 kDa, Sigma-Aldrich), and then fixed
817 on a spherical treadmill. Imaging was done on a Sutter Movable Objective Microscope with a 20X,
818 1.0 NA water dipping objective (Olympus, XLUMPlanFLN). A MaiTai HP (Spectra-Physics,
819 Santa Clara, CA) laser tuned to 800 nm was used for fluorophore excitation. All imaging with the
820 water-immersion lens was done with room-temperature distilled water. All the 2PLSM
821 measurements were started at least 20 minutes after isoflurane exposure to avoid the disruption of
822 physiological signals due to anesthetics.
823 For navigational purposes, wide field images were collected to generate vascular maps of
824 brain pial vascular maps of the entire PoRTS window. We performed three different measurements
825 using 2PLSM. (1) To measure blood vessel diameter responses to locomotion, individual arteries
826 and veins were imaged at nominal frame rate of 3 Hz for 5 minutes using 10-15 mW of power
827 exiting the objective. The diameter of pial vessels were calculated as previously described [65]. (2)
828 To measure RBC velocity and RBC spacing, line scan images were collected from individual
829 capillaries (diameter range: 2-8 µm). The pixel dwell time for the line scan segments was 1 µs and
830 we achieved a ~1.5 kHz sampling rate. (3) To measure the vasculature diameter under
831 physiological conditions (i.e., awake and resting), we collected stack image every other day for
832 each mouse. For each mouse, we collected data from 4 different days and collected 3 different
833 trials on each day. Shortly (within 20 minutes) after the last trial on the last day, the mouse was
834 perfused for future vasculature reconstruction. The resolution for each XY plane is 0.64 µm/pixel
835 and the resolution for Z direction is 1 µm. On the Z-direction, three frames were collected and
836 averaged, the averaged frame was saved in the file. All the images were acquired with increasing
837 laser power up to 100 mW at a depth of ~200 um.
838 *Isoflurane challenge*. To compare the capability of vasodilation in both young and aged
839 mice, we exposed a subset of mice to short period (~ 2 minutes) of isoflurane (5% in pure oxygen)

and imaged the pial vessel (specifically, the branch of the middle cerebral artery) diameter responses. This allowed us to assess the magnitude of diameter change of pial arteries and veins.

Oxygen challenge experiments. In a subset of experiments, hyperoxia was induced by substituting breathing air for 100% pure oxygen. Using optical imaging of spectroscopy, we performed an oxygen challenge. Mice were head-fixed on a spherical treadmill, and a nose cone was fixed ~ 1 inch in front of the nose, with care taken not to contact the whiskers. Two gases were administered during a 5-min spectroscopy trial in the following order: 1 min breathable air (21% oxygen), 3 min 100% oxygen, and 1 min breathable air. Mice breathed breathable air for at least 2 min between trials, to ensure physiological parameters returned to baseline. Reflectance images were collected during periods of green LED light illumination at 530 nm (equally absorbed by oxygenated and deoxygenated hemoglobin, M530L3, Thorlabs) or blue LED light illumination at 470 nm (absorbed more by oxygenated than deoxygenated hemoglobin, M470L3, Thorlabs) or red LED light illumination at 660 nm (absorbed more by deoxygenated than oxygenated hemoglobin, M660L2, Thorlabs).

Data analysis for *in vivo* recording.

All data analyses were performed in Matlab (R2019b, MathWorks) using custom code.

Locomotion event identification. Locomotion events [59,63,111] from the spherical treadmill were identified by first applying a low-pass filter (10 Hz, 5th order Butterworth) to the velocity signal from the optical rotary encoder, and then comparing the absolute value of acceleration (first derivative of the velocity signal) to a threshold of 3 cm/s^2. Periods of locomotion were categorized based on the binarized detection of the treadmill acceleration:

$$\delta(t) = \theta(|a_t| - a_c) = \begin{cases} 1, & |a_t| \geq a_c \\ 0, & |a_t| < a_c \end{cases}$$

where a_t is the acceleration at time t, and a_c is the treadmill acceleration threshold.

Spontaneous activity. To characterize spontaneous (non-locomotion-evoked) activity, we defined "resting" periods as periods started 4 seconds after the end of previous locomotion event and lasting no less than 60 seconds.

Calculation of hemodynamic response function. We considered the neurovascular relationship to be a linear time invariant system [75,113,114]. To provide a model-free approach to assess the relationship between CBV or vessel diameter and neural activity, hemodynamic response function (HRF) was calculated by deconvoluting CBV signal, oxygen signal or vessel diameter signal to locomotion events, respectively, using the following equation:

$$\mathrm{H}_{(k+1)\times 1} = (\mathrm{L}^{\mathrm{T}}\mathrm{L})^{-1}\mathrm{L}^{\mathrm{T}}\mathrm{V}_{(m+k)\times 1}$$

H is the HRF, V is the tissue oxygenation signal or neural activity signal. L is a Toeplitz matrix of size (m+k) x (k+1) containing binarized locomotion events (n):

$$\mathrm{L}(\vec{\mathrm{n}}) = \begin{pmatrix} 1 & \mathrm{n}_1 & 0 & 0 & \cdots & 0 \\ 1 & \mathrm{n}_2 & \mathrm{n}_1 & 0 & \cdots & 0 \\ \vdots & \vdots & \mathrm{n}_2 & \mathrm{n}_1 & \cdots & \vdots \\ \vdots & \mathrm{n}_k & \vdots & \mathrm{n}_2 & \cdots & \mathrm{n}_1 \\ \vdots & 0 & \mathrm{n}_k & \vdots & \cdots & \mathrm{n}_2 \\ \vdots & \vdots & \vdots & \mathrm{n}_k & \ddots & \vdots \\ 1 & 0 & 0 & 0 & \cdots & \mathrm{n}_k \end{pmatrix}$$

Comparison of HRF parameters. To quantify the temporal features of HRF, the HRF for CBV was fitted using a gamma-variate fitting process [75,115–118] using a gamma-variate function kernel of the following form,

$$\mathrm{HRF}(t, T, W, A) = A * (\frac{t}{T})^{\alpha} * e^{(\frac{t-T}{-\beta})},$$

where $\alpha = (T/W)^2 * 8.0 * \log(2.0)$, $\beta = W^2/(T * 8.0 * \log(2.0))$. For modeling HRF using a gamma-variate function kernel, we used a downhill simplex algorithm minimizing the sum square difference between measured and predicted hemodynamics. The goodness of fit was quantified as $R^2 = 1 - \frac{\sum(HRF_{actual} - HRF_{model})^2}{\sum(HRF_{actual} - \overline{HRF})^2}$, where $\overline{HRF}$ is the mean value of the actual HRF. To quantify the amplitude of each HRF, we used the value at the peak of the modeled HRF. Time to peak (TTP) was calculated as the time at which the modeled HRF reached its maximum amplitude. Full-width at half maximum (FWHM) was defined as the time from which the modeled HRF rose to 50% of its peak until it fell to 50% of its peak. TTP, FWHM and HRF amplitudes across different cortical depths were compared using a linear model to quantify trends (robustfit, MATLAB).

2PLSM image processing. (1) To quantify blood vessel diameter responses to locomotion, individual frames from 2PLSM imaging were aligned using a rigid registration algorithm to remove motion artifacts in the x–y plane [65]. Visual inspection of movies indicated that there was minimal z-axis motion. A rectangular box was manually drawn around a short segment of the vessel and the pixel intensity was averaged along the long axis [65]. Pixel intensity was used to calculate diameter from the full-width at half-maximum. Periods of rest were segregated using locomotion events measured with the rotary encoder. For each 5-min trial, diameter measurements were normalized to the average diameter during periods of rest. The diameters were smoothed with a third-order, 15-point Savitzky–Golay filter (Matlab function: sgolayfilt). (2) To quantify RBC velocity, blood flow velocity was calculated using Radon transform [64]. Only blood flow velocity during resting periods was reported. Capillary diameter was manually measured using ImageJ software. To quantify RBC spacing, we utilized the method reported in our previous study [61]. We identified RBC "stall" events as an inter-RBC spacing greater than 1 second. We only used RBCs spacing intervals during relatively long resting segments (i.e., ≥ 5 second). (3) As the perfusion procedure and brain fixation might affect the brain vasculature [119], to compare our measurements for vessel radii in STPT and LSFM imaging datasets to vessel parameters measured in vivo using 2PLSM, the same animals that were used for 2PLSM and STPT imaging were reconstructed and compared, as described before [29].

Statistical analysis

For the STPT and LSFM datasets, we used Matlab (Mathworks) and/or Prism (Graphpad) for all statistical analysis, including multi-region of interest (ROI) correlation analysis. Data was organized in Prism using grouped analysis with each individual animal included in sub columns within each age group. Grouped analysis also allowed for comparisons between brain regions, with each brain region included as a row replicate. All data were reported as the mean ± standard deviation (SD), while treating each anatomical subregion (ROI) as an individual data point. For two group comparisons, multiple unpaired t-tests were used with multiple comparison correction to correct for comparisons across multiple brain regions. The p-value was adjusted with the false discovery rate for multiple comparison corrections using the Two-stage step-up method of Benjamini, Krieger and Yekutieli in Graphpad. For multiple group comparisons, two-way ANOVA, or mixed model if including NaN values, to generate comparison between groups using Prism. Scatter plots were generated with Matlab, all other graphs were generated with Prism version 9 software.

For *in vivo* recording, all summary data were reported as the mean ± standard deviation (SD) unless stated otherwise. The normality of the samples was tested before statistical testing using the Anderson-Darling test (adtest). For comparison of multiple populations, the assumption of equal variance for parametric statistical method was also tested (vartest2). If criteria of normality and equal variance were not met, parametric tests (unpaired t test) were replaced with a nonparametric method (Wilcoxon rank sum test). For comparisons of oxygen challenge and isoflurane challenge effects on brain hemodynamics across different age groups, we used the linear mixed effect model (MATLAB function: fitlme). Significance was accepted at $p < 0.05$.

Figures

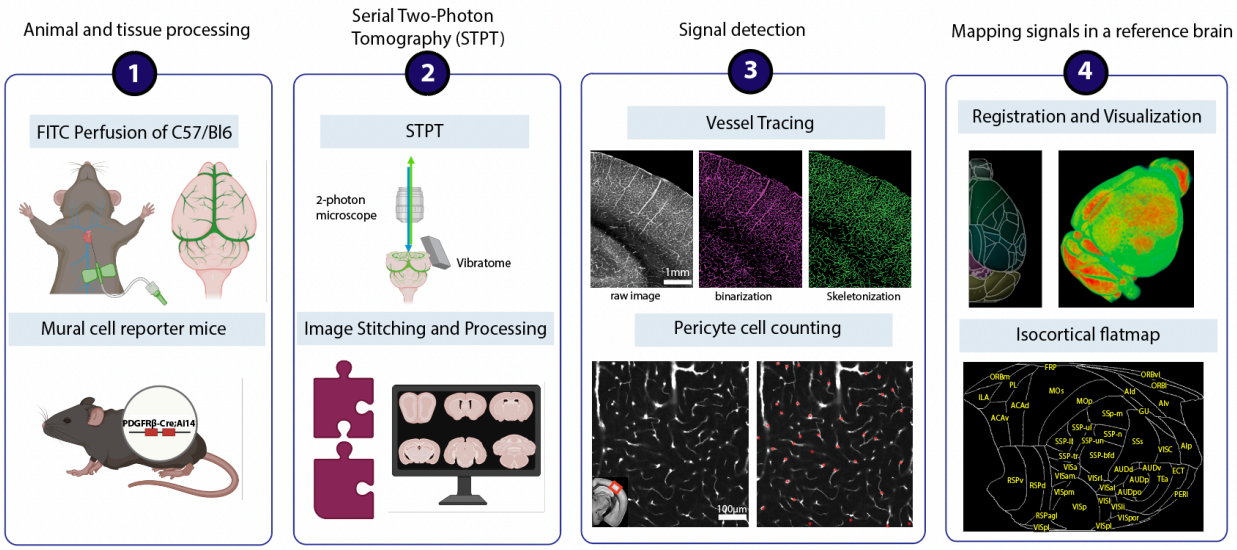

Figure 1. STPT based vessel tracing and pericyte counting pipeline
The steps of the STPT pipeline are outlined in order. **1**. Brain sample collection: vascular filling procedure via cardiac perfusion with FITC conjugated albumin gel and pericyte mapping using PDGFRβ-Cre;Ai14 reporter mice. **2**. STPT imaging: combination of 2-photon microscope 2D tile imaging with serial vibratome sectioning to obtain cellular resolution images of the whole mouse brain. These image tiles are then stitched to reconstruct tissue sections spanning the olfactory bulb to the cerebellum. **3**. Signal detection: vascular tracing with binarization of FITC filled vascular signals and skeletonization, and deep learning-based detection of capillary pericytes. **4**. Mapping signals in a reference brain: All detected signals were registered to the Allen Common Coordinate Framework (Allen CCF) and an isocortical flatmap was used to examine signals in the isocortex.

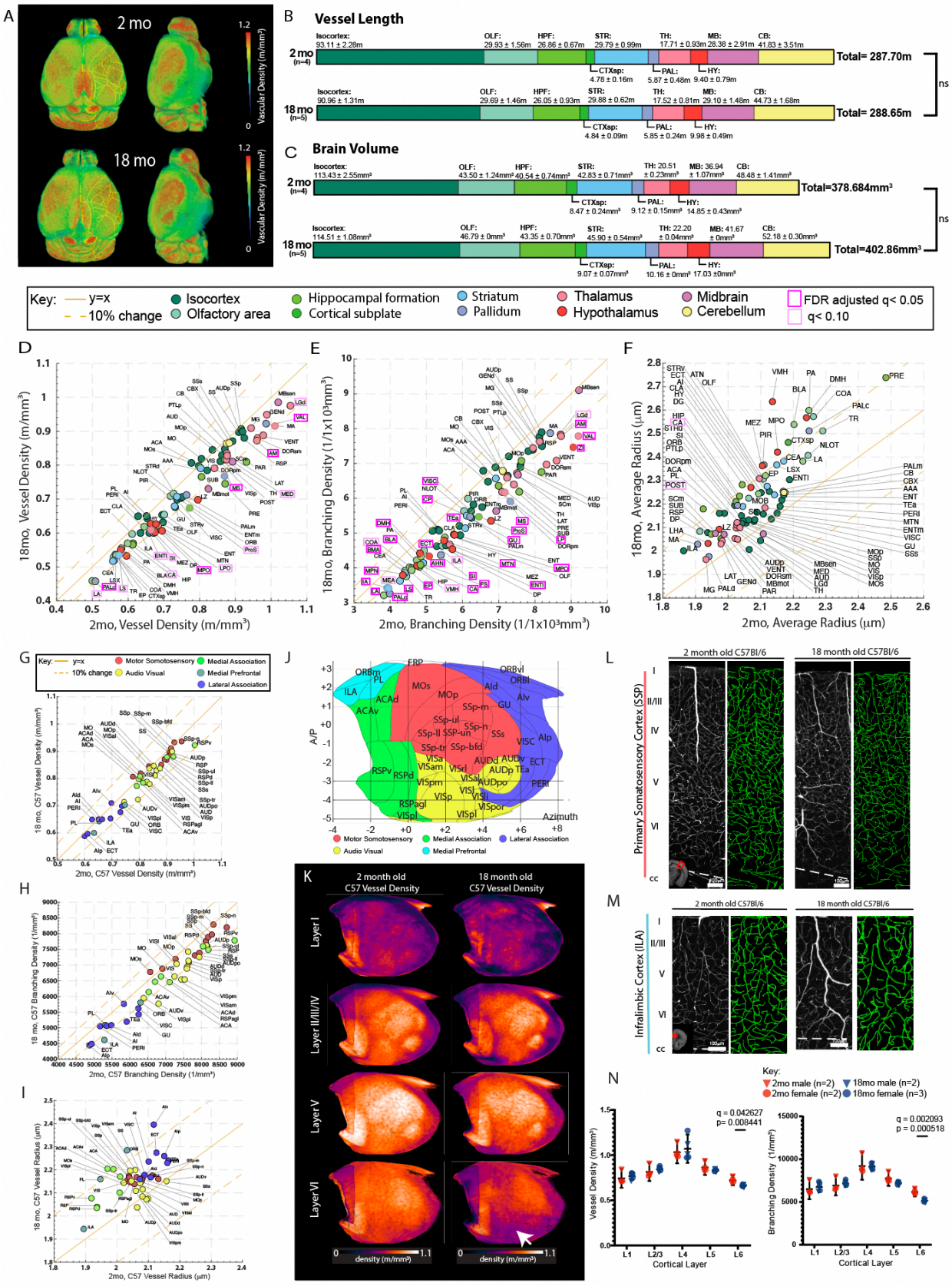
A
2 mo
18 mo
Vascular Density (m/mm³)
B
Vessel Length
2 mo (n=4)
Isocortex: 93.11 ± 2.28m
OLF: 29.93 ± 1.56m
HPF: 26.86 ± 0.67m
STR: 29.79 ± 0.99m
TH: 17.71 ± 0.93m
MB: 28.38 ± 2.91m
CB: 41.83 ± 3.51m
CTXsp: 4.78 ± 0.16m
PAL: 5.87 ± 0.48m
HY: 9.40 ± 0.79m
Total= 287.70m
18 mo (n=5)
Isocortex: 90.96 ± 1.31m
OLF: 29.69 ± 1.46m
HPF: 26.05 ± 0.93m
STR: 29.88 ± 0.62m
TH: 17.52 ± 0.81m
MB: 29.10 ± 1.48m
CB: 44.73 ± 1.68m
CTXsp: 4.84 ± 0.09m
PAL: 5.85 ± 0.24m
HY: 9.98 ± 0.49m
Total= 288.65m
ns
C
Brain Volume
2 mo (n=4)
Isocortex: 113.43 ± 2.55mm³
OLF: 43.50 ± 1.24mm³
HPF: 40.54 ± 0.74mm³
STR: 42.83 ± 0.71mm³
TH: 20.51 ± 0.23mm³
MB: 36.94 ± 1.07mm³
CB: 48.48 ± 1.41mm³
CTXsp: 8.47 ± 0.24mm³
PAL: 9.12 ± 0.15mm³
HY: 14.85 ± 0.43mm³
Total=378.684mm³
18 mo (n=5)
Isocortex: 114.51 ± 1.08mm³
OLF: 46.79 ± 0mm³
HPF: 43.35 ± 0.70mm³
STR: 45.90 ± 0.54mm³
TH: 22.20 ± 0.04mm³
MB: 41.67 ± 0mm³
CB: 52.18 ± 0.30mm³
CTXsp: 9.07 ± 0.07mm³
PAL: 10.16 ± 0mm³
HY: 17.03 ±0mm³
Total=402.86mm³
ns
Key:
y=x
10% change
Isocortex
Olfactory area
Hippocampal formation
Cortical subplate
Striatum
Pallidum
Thalamus
Hypothalamus
Midbrain
Cerebellum
FDR adjusted q< 0.05
q< 0.10
D
18mo, Vessel Density (m/mm³)
2mo, Vessel Density (m/mm³)
E
18mo, Branching Density (1/1x10³mm³)
2mo, Branching Density (1/1x10³mm³)
F
18mo, Average Radius (µm)
2mo, Average Radius (µm)
G
Key:
y=x
10% change
Motor Somotosensory
Audio Visual
Medial Association
Medial Prefrontal
Lateral Association
18 mo, C57 Vessel Density (m/mm³)
2mo, C57 Vessel Density (m/mm³)
H
18 mo, C57 Branching Density (1/mm³)
2mo, C57 Branching Density (1/mm³)
I
18 mo, C57 Vessel Radius (µm)
2mo, C57 Vessel Radius (µm)
J
A/P
Azimuth
Motor Somotosensory
Audio Visual
Medial Association
Medial Prefrontal
Lateral Association
K
2 month old C57 Vessel Density
18 month old C57 Vessel Density
Layer I
Layer II/III/IV
Layer V
Layer VI
density (m/mm³)
L
2 month old C57Bl/6
18 month old C57Bl/6
Primary Somatosensory Cortex (SSP)
I
II/III
IV
V
VI
cc
M
2 month old C57Bl/6
18 month old C57Bl/6
Infralimbic Cortex (ILA)
I
II/III
V
VI
cc
N
Key:
2mo male (n=2)
18mo male (n=2)
2mo female (n=2)
18mo female (n=3)
q = 0.042627
p= 0.008441
Vessel Density (m/mm³)
Cortical Layer
q = 0.002093
p = 0.000518
Branching Density (1/mm³)
Cortical Layer

Figure 2. Region specific reduction of vascular length and branching density and increased vascular radii

(**A**) The averaged vasculature length density of 2-month-old (N=4) and 18-month-old (N=5) brains registered to the Allen CCF. (**B-C**) Summed vessel length (**B**) and brain volume (**C**) in 2-month-old and 18-month-old brains with the mean and SD provided for each anatomical region. (**D-F**) Scatter plots of averaged vascular length density (m/mm^3) (**D**), vascular branching density ($1/mm^3$) (**F**), and vascular radii (μm) between 2-month-old (x axis) and 18-month-old (y axis) brains across different brain regions. Areas that reach FDR adjusted $q < 0.05$ are outlined in magenta boxes. (**G-I**) Scatter plots of the isocortex data for averaged vascular length density (**G**), vascular branching density (**H**), vascular radii (**I**) between 2-month-old (x axis) and 18-month-old (y axis) brains. Isocortical areas are color coded based on grouping in **J**. The solid yellow line represents y=x and the dotted line on either side represents a 10% difference from the solid yellow line. No areas show significant changes. (**J**) Isocortical flatmap with Allen CCF border lines and region-based color-coding. Y axis: Bregma anterior-posterior (A-P) coordinates, X axis: the azimuth coordinate represents the physical distance by tracing the cortical surface on the coronal cut. (**K**) Averaged vascular length density of different cortical layers in the flatmap between 2-month-old and 18-month-old brains. A white arrow highlights the significant decrease of vascular length density in the layer 6 cortical layers. (**L-M**) 250μm maximum intensity projection images of the primary somatosensory cortex (**L**) and the infralimbic cortex (**M**) with vascular tracing (green on the right side) between 2-month-old and 18-month-old brains. Note the significant reduction of vasculature in the deep layer. (**N**) Both vascular length and branching density showed significant reductions in layer 6. Brain region abbreviations can be found in Supplementary Data 1 or Allen atlas at https://atlas.brain-map.org/atlas?atlas=602630314.

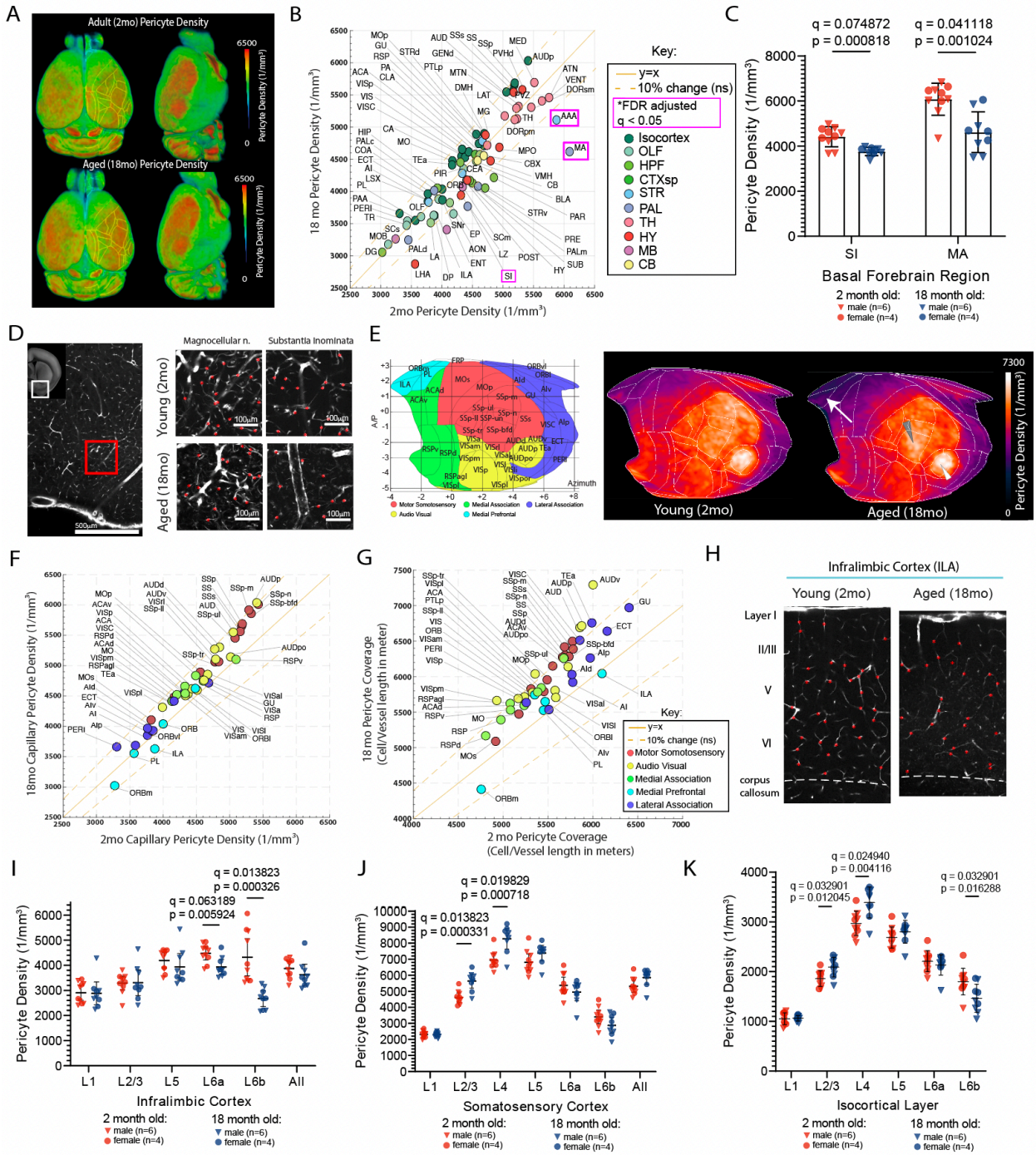

Figure 3. Aged brain showed selective reduction of capillary pericytes in the basal forebrain area and the deep cortical layer

(**A**) Averaged capillary pericyte density in 2-month-old (n=10) and 18-month-old (n=9) PDGFRβ-Cre;Ai14 mouse brains that are registered to the Allen CCF. (**B**) A scatter plot of capillary pericyte density between 2-month-old (x axis) and 18-month-old (y axis). Brain areas are color coded based on the Allen CCF ontology. Brain regions that are significantly different between groups, reflected by FDR adjusted q<0.05, are outlined in magenta boxes. The solid yellow line represents the value for y=x and the yellow dotted lines on either side of the solid yellow line represent a 10% difference from the solid yellow line. (**C**) Bar graphs of capillary

979 pericyte density in the substantia innominata and magnocellular nucleus between 2-month-old
980 and 18-month-old brains. (**D**) Representative images of the basal forebrain (left) and higher
981 resolution examples of the magnocellular nucleus and substantia innominata in 2-month-old and
982 18-month-old brains. Red dots represent detected pericyte cell bodies in each respective region.
983 (**E**) The isocortical flatmap (left) and averaged capillary pericyte densities plotted in the flatmap
984 from 2-month-old and 18-month-old brains. (**F-G**) Scatter plots of capillary pericyte density (**F**)
985 and pericyte coverage (pericyte density per vascular length density; **G**) in isocortical areas. (**H**)
986 Representative images of capillary pericyte density in the infralimbic cortex from 2-month-old
987 and 18-month-old brains. (**I-K**) Layer specific capillary pericyte densities from the infralimbic
988 cortex (**I**), the somatosensory cortex (**J**), and across all isocortical areas (**K**). Note the significant
989 density reduction in the deep cortical layers. All q values obtained from multiple comparison
990 correction by false discovery rate are reported in each graph as well as the uncorrected p-value.
991 See Supplementary Data 2 for full data.
992

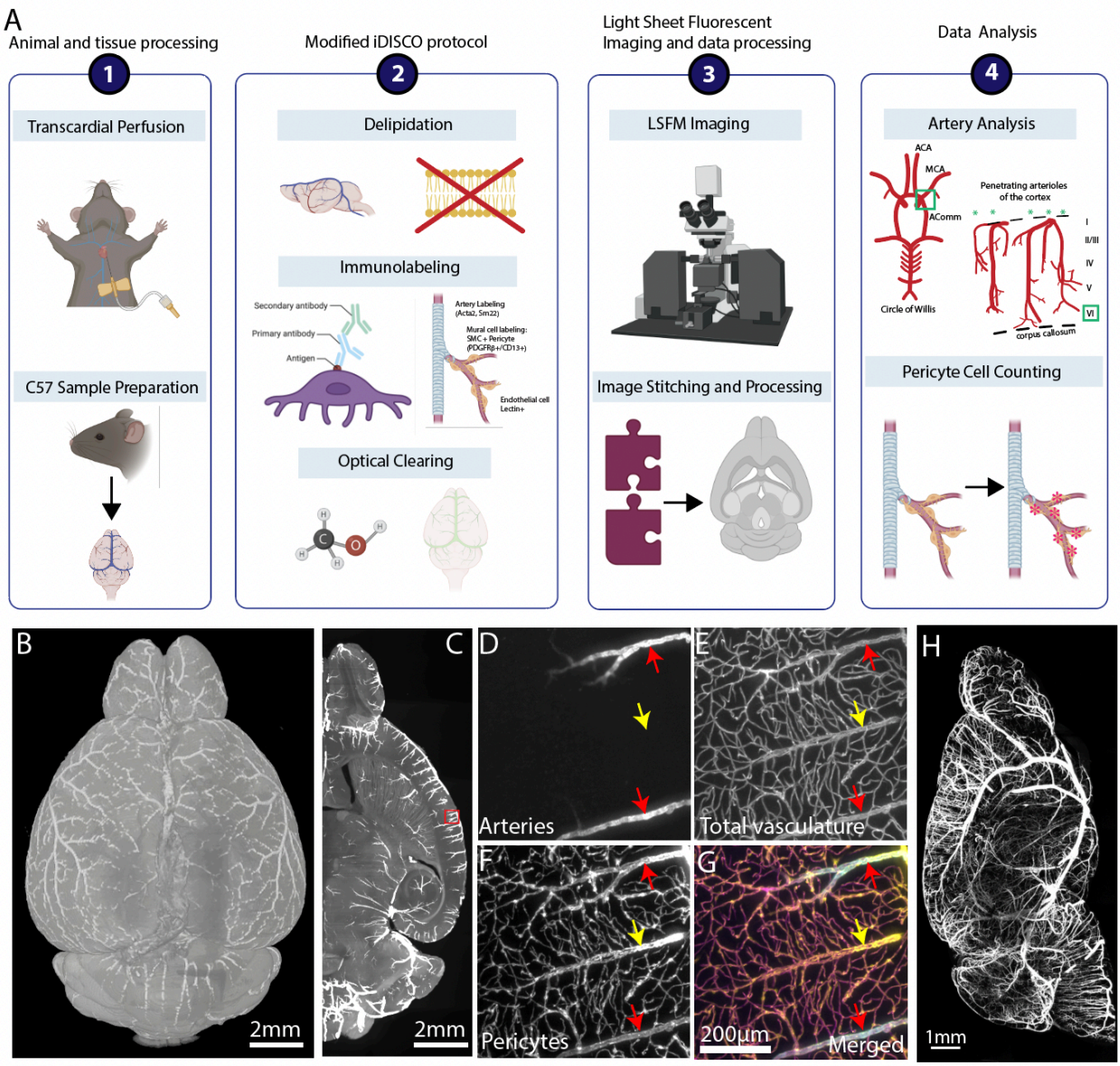

Figure 4. Tissue clearing and 3D immunolabeling with LSFM imaging to examine different vascular compartments and mural cells in the same brain

(**A**) The steps of brain clearing, whole brain immunolabeling, and light sheet fluorescent microscopy (LSFM) pipeline are outlined in order. **1**. Brain sample collection with transcardial perfusion. **2**. Modified iDISCO protocol including delipidation, immunolabeling for arteries, whole vasculature, and pericytes, and optical clearing. **3**. LSFM imaging and data processing to visualize cleared brains at cellular resolution. **4**. Data analysis such as arteriole geometry analysis and pericyte counting. (**B**) 3D reconstruction of a brain with artery staining by LSFM imaging. (**C**) Max projection of the 500 µm thick z stack of the artery staining. (**D-G**) Zoom-in images of the red box area from (**C**). (**D**) artery staining in the green channel, (**E**) lectin based total vasculature staining in the red channel, (**F**) pericyte staining in the far-red channel, (**G**) a merged image of pseudo-colored arteries (blue), total vasculature (green), and pericyte (red). (**H**) Maximum projection of the artery channel in a brain hemisphere.

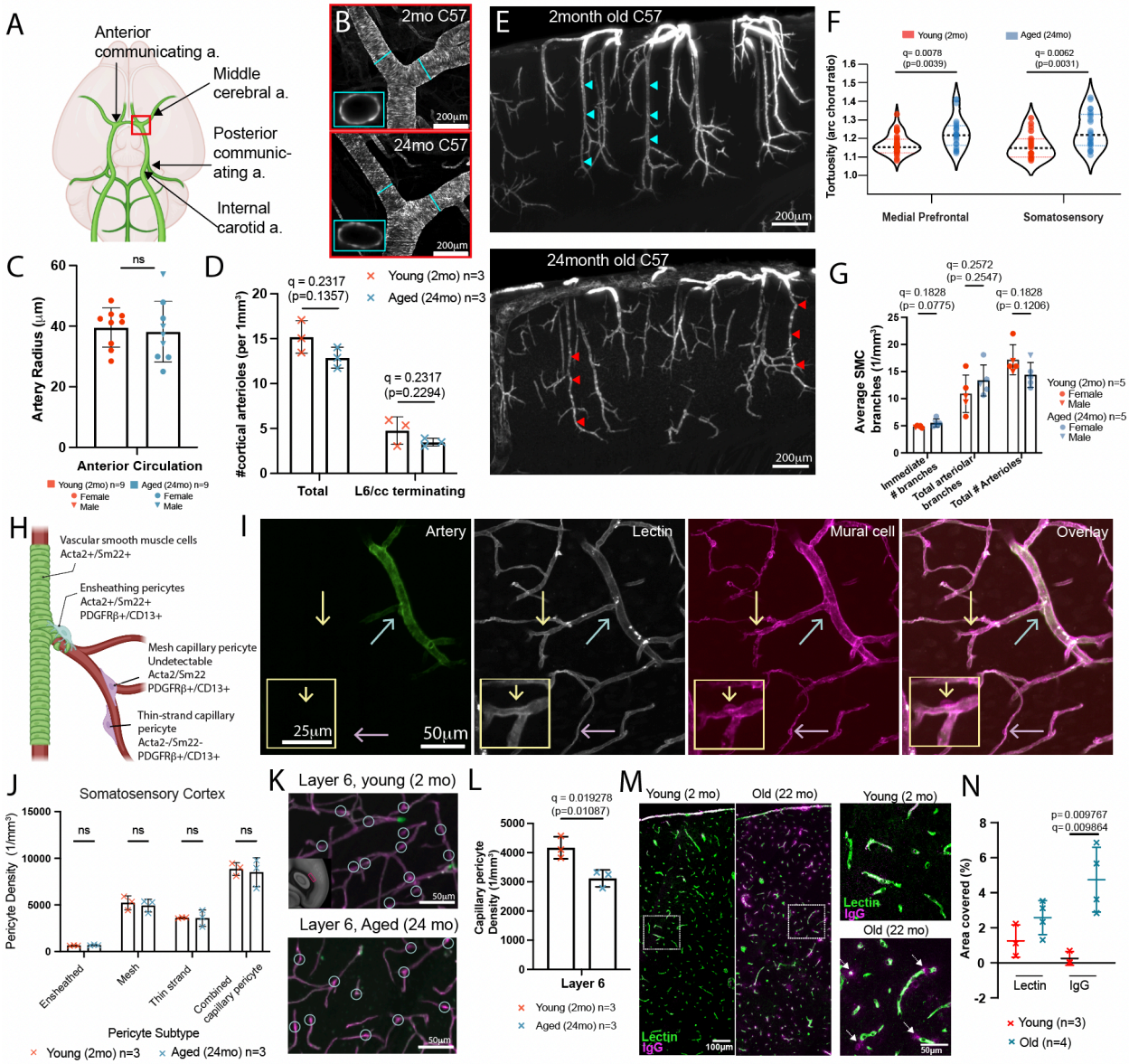

Figure 5. Aging induces significant arteriole remodeling and selective pericyte density reduction.

(**A**) Schema of main arteries of the circle of Willis at the ventral surface of the brain. (**B**) Artery specific labeling of the middle cerebral artery branching area (red box area in H) from 2-month-old and 24-month-old brains. (**C**) Artery radii do not show a significant difference between the two age groups. (**D**) The number of both total and deep layer 6 reaching penetrating cortical arteriole did not show a significant difference between the two age groups. (**E**) Representative 600 µm MIPs of artery labeling in the somatosensory area of a young (top) and an aged (bottom) brain. Note tortuous arterioles in the old brain (red arrowheads) compared to straight ones in the young brain (light blue arrowheads). (**F**) Old brains showed significantly tortuous arterioles in the medial prefrontal and somatosensory cortices. Data from 3 animals for both young and aged groups. (**G**) Both immediate and total arteriole branch numbers show no significant differences between the two age groups. (**H**) Different pericyte subtypes with immuno markers and their position in the vascular order. (**I**) Submicron resolution LSFM images with artery labeling,

1023 whole vasculature labeled with lectin and mural cell labeling with PDGFRβ and CD13
1024 antibodies. The cyan arrow for an ensheathing pericyte, the yellow arrow for a mesh capillary
1025 pericyte, and the purple arrow for a thin-strand capillary pericyte. (**J**) Manual cell counting did
1026 not show any significant difference in the somatosensory cortex between the two age groups. (**K-**
1027 **L**) However, layer 6 of the somatosensory cortex (**K**) showed a significant reduction in pericyte
1028 density (**L**). (**M-N**) Increased IgG extravasation in 22-month-old brain compared to 2-month-old
1029 brain (**M**) and quantification (**N**). All q values obtained from multiple comparison correction by
1030 false discovery rate and uncorrected p-value are reported in each graph, except (F) with
1031 Bonferroni correction.
1032

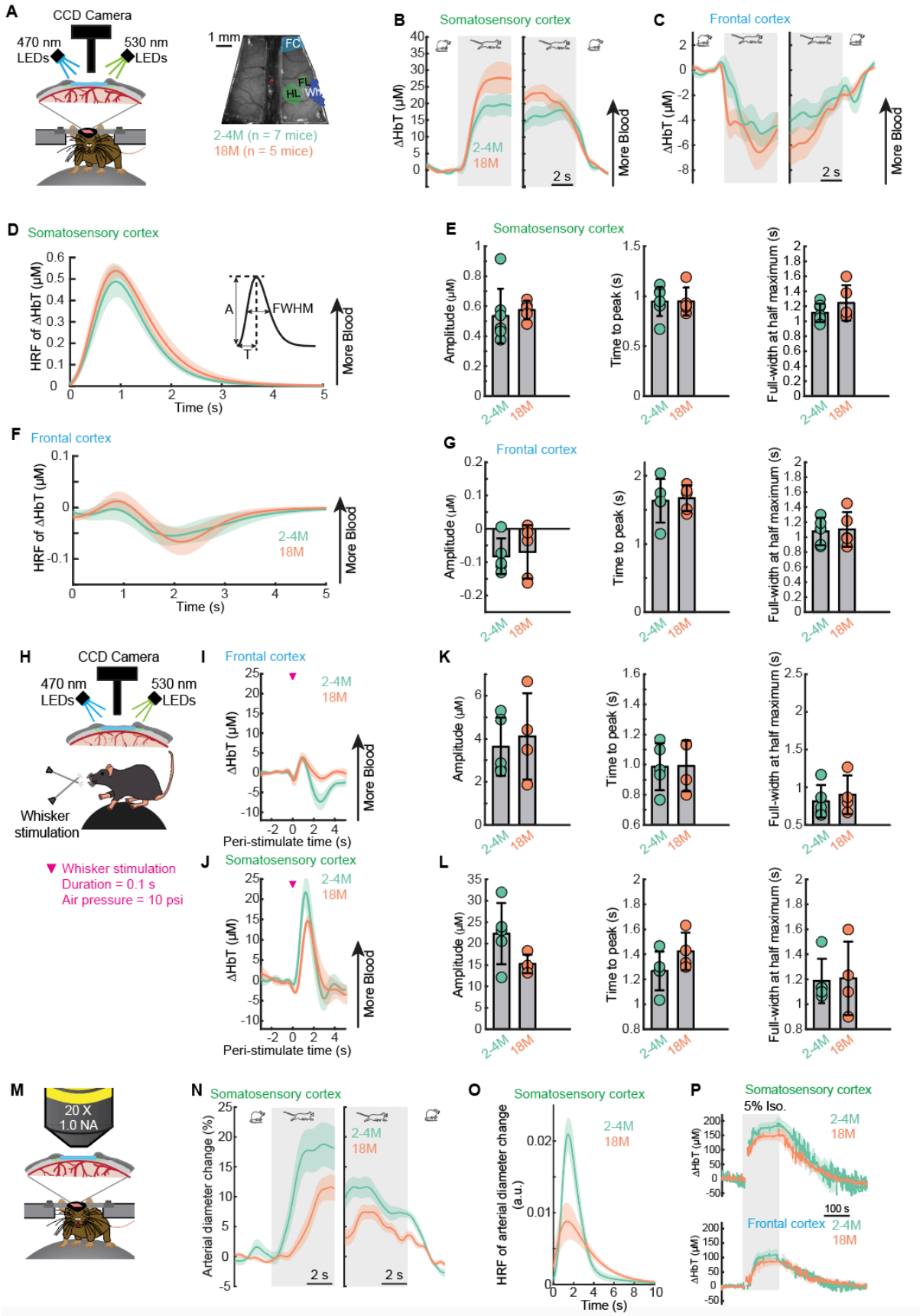
A
CCD Camera
470 nm LEDs
530 nm LEDs
1 mm
FC
FL
HL
Wh
2-4M (n = 7 mice)
18M (n = 5 mice)
B
Somatosensory cortex
ΔHbT (μM)
2-4M
18M
2 s
More Blood
C
Frontal cortex
ΔHbT (μM)
2 s
More Blood
D
Somatosensory cortex
HRF of ΔHbT (μM)
A
FWHM
T
Time (s)
More Blood
E
Somatosensory cortex
Amplitude (μM)
Time to peak (s)
Full-width at half maximum (s)
2-4M
18M
F
Frontal cortex
HRF of ΔHbT (μM)
2-4M
18M
Time (s)
More Blood
G
Frontal cortex
Amplitude (μM)
Time to peak (s)
Full-width at half maximum (s)
2-4M
18M
H
CCD Camera
470 nm LEDs
530 nm LEDs
Whisker stimulation
▼ Whisker stimulation
Duration = 0.1 s
Air pressure = 10 psi
I
Frontal cortex
2-4M
18M
ΔHbT (μM)
More Blood
Peri-stimulate time (s)
J
Somatosensory cortex
2-4M
18M
ΔHbT (μM)
More Blood
Peri-stimulate time (s)
K
Amplitude (μM)
Time to peak (s)
Full-width at half maximum (s)
2-4M
18M
L
Amplitude (μM)
Time to peak (s)
Full-width at half maximum (s)
2-4M
18M
M
20 X
1.0 NA
N
Somatosensory cortex
Arterial diameter change (%)
2-4M
18M
2 s
2 s
O
Somatosensory cortex
HRF of arterial diameter change (a.u.)
2-4M
18M
Time (s)
P
Somatosensory cortex
5% Iso.
2-4M
18M
ΔHbT (μM)
100 s
Frontal cortex
2-4M
18M
ΔHbT (μM)

1033

1034 **Figure 6. Cortical hemodynamic responses to voluntary locomotion and whisker stimulation**
1035 **is intact in normal aging.**
1036 (**A**) Left, schematic of the experimental setup for IOS imaging during voluntary locomotion. Right,
1037 an image of thin-skull window and overlay of corresponding anatomical reconstruction; scale bar
1038 = 1 mm. FC, frontal cortex; FL/HL, forelimb/hindlimb representation of the somatosensory cortex;
1039 Wh, vibrissae cortex. (**B**) Population average of locomotion onset (left) and offset (right) triggered
1040 average of ΔHbT responses in FL/HL across different age groups. (**C**) As in (**B**) but for FC. (**D**)
1041 Hemodynamic response function (HRF) of ΔHbT in the FL/HL across different age groups. (**E**)
1042 Quantification of HRF of ΔHbT in the FL/HL: amplitude (A, left), time to peak (T, middle), and
1043 full-width at half maximum (FWHM, right). (**F**) As in (**D**) but for FC. (**G**) As in (**E**) but for FC.
1044 (**H**) Schematic of the experimental setup for IOS imaging during whisker stimulation. (**I**) Average
1045 population responses of ΔHbT to contralateral whisker stimulation in the FL/HL across different
1046 age groups. (**J**) Quantification of the whisker stimulation evoked responses of ΔHbT in the FL/HL:
1047 amplitude (left), time to peak (middle) and full-width at half maximum (right). (**K**) As in (**I**) but
1048 for FC. (**L**) As in (**J**) but for FC. (**M**) Schematic of the experimental setup for 2PLSM imaging
1049 during locomotion. (**N**) Population average of locomotion onset (left) and offset (right) triggered
1050 average of arteriole diameter responses in FL/HL across different age groups. (**O**) Hemodynamic
1051 response function (HRF) of arteriole diameter changes in the FL/HL across different age groups.
1052 (**P**) Population average of ΔHbT responses to inhalation of 5% isoflurane in the FL/HL (top) and
1053 FC (bottom) across different age groups. Solid lines and shaded areas in (**B**, **C**, **D**, **F**, **I**, **N**, **O, P**)
1054 denote mean ± SEM, respectively. Data are shown as mean ± SD in all other graphs.
1055

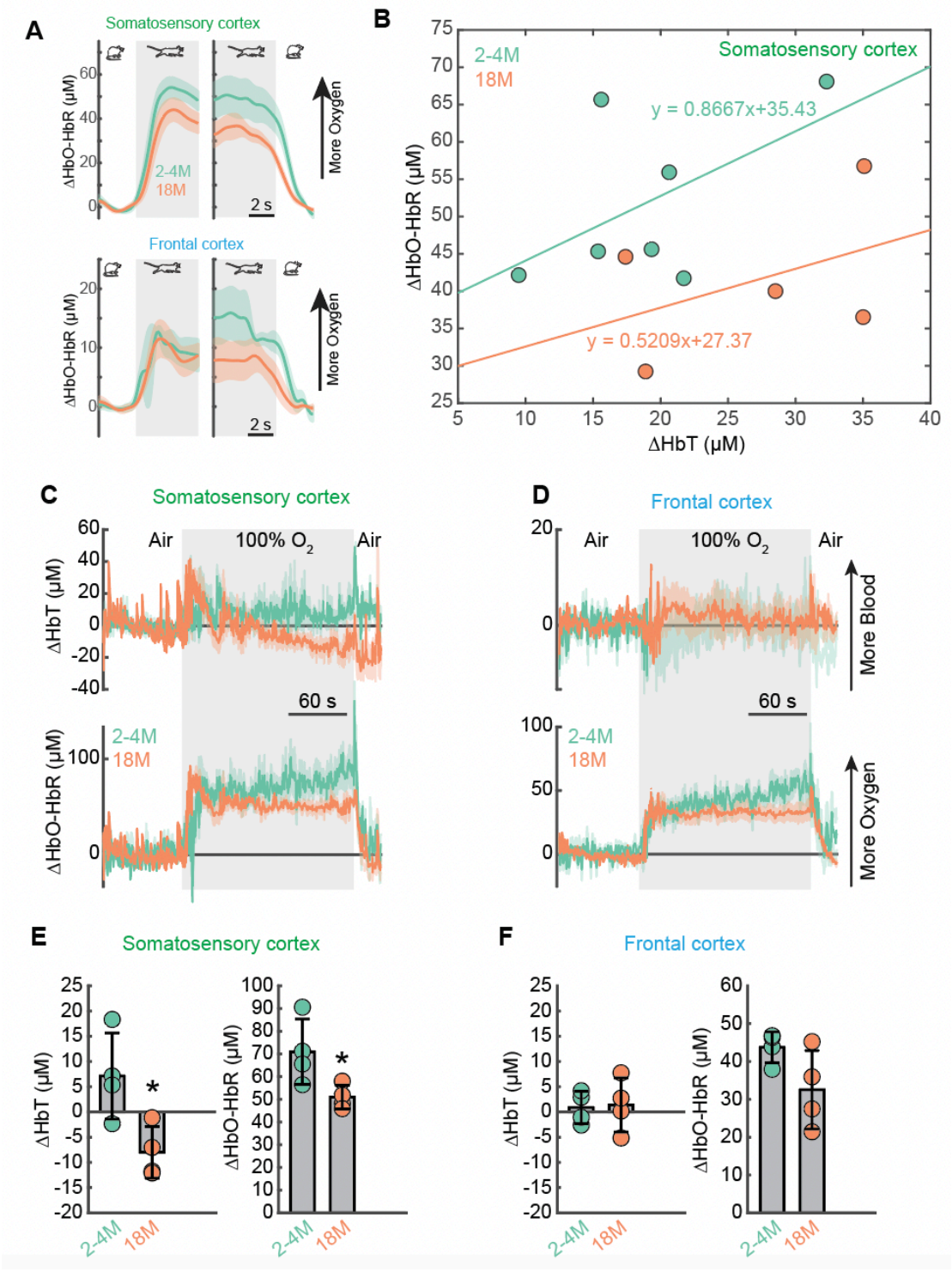

Figure 7. Oxygen carrying capacity of the blood is reduced by aging.
(**A**) Population average of locomotion onset and offset triggered average of brain oxygenation (ΔHbO-HbR) responses in FL/HL and FC across different age groups. (**B**) Relationship between locomotion evoked change in ΔHbT and ΔHbO-HbR, 2-5 s after the onset of locomotion, across different age groups, in FL/HL. (**C**) Population average of ΔHbT (top) and ΔHbO-HbR (bottom) responses to inhalation of 100% oxygen in the FL/HL across different age groups. (**D**) As in (**C**)

1063 but for FC. (**E**) Group average of fractional changes of ΔHbT (left) and ΔHbO-HbR (right) in
1064 response to 100% oxygen in FL/HL across different age groups. * p-value <0.05. (**F**) As in (**E**) but
1065 for FC. Solid lines and shaded areas in (**A**, **C**, **D**) denote mean ± SEM, respectively. Data are
1066 shown as mean ± SD in all other graphs.
1067

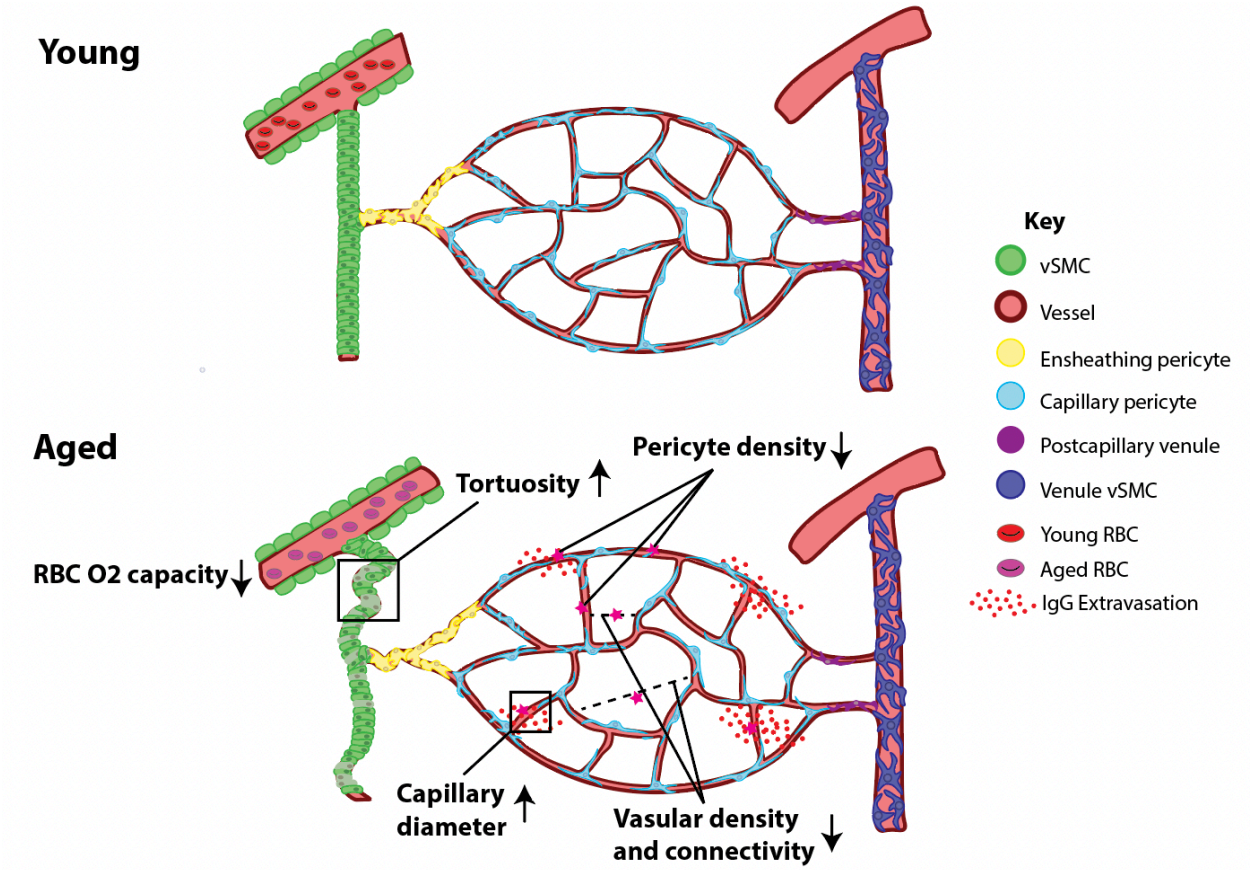

Figure 8. Summary of changes in aged brains

Aged brains show reduced vascular length and branching density, increased radii, reduced pericyte density, leaky BBB, and lower oxygen carrying capacity in the blood compared to young brains.

1074 **References**

1075 1. Lu, H. *et al.* Alterations in cerebral metabolic rate and blood supply across the adult lifespan.
1076 *Cereb Cortex* **21**, 1426–1434 (2011).
1077 2. Pfister, F. *et al.* Pericyte migration: A novel mechanism of pericyte loss in experimental
1078 diabetic retinopathy. *Diabetes* (2008) doi:10.2337/db08-0325.
1079 3. Brown, W. R. & Thore, C. R. Review: Cerebral microvascular pathology in ageing and
1080 neurodegeneration. *Neuropathology and Applied Neurobiology* **37**, 56–74 (2011).
1081 4. Baloyannis, S. J. & Baloyannis, I. S. The vascular factor in Alzheimer's disease: A study in
1082 Golgi technique and electron microscopy. *Journal of the Neurological Sciences* **322**, 117–
1083 121 (2012).
1084 5. Almeida, V. M. *et al.* Pericytes Make Spinal Cord Breathless after Injury. *Neuroscientist* **24**,
1085 440–447 (2018).
1086 6. Hayden. Type 2 Diabetes Mellitus Increases The Risk of Late-Onset Alzheimer's Disease:
1087 Ultrastructural Remodeling of the Neurovascular Unit and Diabetic Gliopathy. *Brain*
1088 *Sciences* **9**, 262 (2019).
1089 7. Abrahamson, E. E. & Ikonomovic, M. D. Brain injury-induced dysfunction of the blood brain
1090 barrier as a risk for dementia. *Experimental Neurology* **328**, 113257 (2020).
1091 8. Uemura, M. T., Maki, T., Ihara, M., Lee, V. M. Y. & Trojanowski, J. Q. Brain Microvascular
1092 Pericytes in Vascular Cognitive Impairment and Dementia. *Front. Aging Neurosci.* **12**, 80
1093 (2020).
1094 9. Iadecola, C. *et al.* The Neurovasculome: Key Roles in Brain Health and Cognitive
1095 Impairment: A Scientific Statement From the American Heart Association/American Stroke
1096 Association. *Stroke* **0**, (2023).

1097 10. Kapogiannis, D. & Mattson, M. P. Disrupted energy metabolism and neuronal circuit
1098 dysfunction in cognitive impairment and Alzheimer's disease. *Lancet Neurol* **10**, 187–198
1099 (2011).
1100 11. Cunnane, S. C. *et al.* Brain energy rescue: an emerging therapeutic concept for
1101 neurodegenerative disorders of ageing. *Nat Rev Drug Discov* **19**, 609–633 (2020).
1102 12. Nedergaard, M. & Goldman, S. A. Glymphatic failure as a final common pathway to
1103 dementia. *Science* **370**, 50–56 (2020).
1104 13. Hartmann, D. A., Coelho-Santos, V. & Shih, A. Y. Pericyte Control of Blood Flow Across
1105 Microvascular Zones in the Central Nervous System. *Annu Rev Physiol* **84**, 331–354
1106 (2022).
1107 14. Sweeney, M. D., Zhao, Z., Montagne, A., Nelson, A. R. & Zlokovic, B. V. Blood-Brain
1108 Barrier: From Physiology to Disease and Back. *Physiological reviews* **99**, 21–78 (2019).
1109 15. Hartmann, D. A. *et al.* Brain capillary pericytes exert a substantial but slow influence on
1110 blood flow. *Nature Neuroscience* **24**, 633–645 (2021).
1111 16. Bell, R. D. *et al.* Pericytes control key neurovascular functions and neuronal phenotype in
1112 the adult brain and during brain aging. *Neuron* **68**, 409–427 (2010).
1113 17. Yang, T., Sun, Y., Lu, Z., Leak, R. K. & Zhang, F. The impact of cerebrovascular aging on
1114 vascular cognitive impairment and dementia. *Ageing Res Rev* **34**, 15–29 (2017).
1115 18. *Pericyte Biology in Disease*. vol. 1147 (Springer International Publishing, 2019).
1116 19. Ding, R. *et al.* Loss of capillary pericytes and the blood–brain barrier in white matter in
1117 poststroke and vascular dementias and Alzheimer's disease. *Brain Pathol.* **30**, 1087–1101
1118 (2020).

1119 20. Li, Y. *et al.* Aging-associated changes in cerebral vasculature and blood flow as determined
1120 by quantitative optical coherence tomography angiography. *Neurobiology of Aging* **70**,
1121 148–159 (2018).
1122 21. Tarumi, T. & Zhang, R. Cerebral Blood Flow in Normal Aging Adults: Cardiovascular
1123 Determinants, Clinical Implications, and Aerobic Fitness. *J Neurochem* **144**, 595–608
1124 (2018).
1125 22. Juttukonda, M. R. *et al.* Characterizing cerebral hemodynamics across the adult lifespan with
1126 arterial spin labeling MRI data from the Human Connectome Project-Aging. *Neuroimage*
1127 **230**, 117807 (2021).
1128 23. Sweeney, M. D., Kisler, K., Montagne, A., Toga, A. W. & Zlokovic, B. V. The role of brain
1129 vasculature in neurodegenerative disorders. *Nature Neuroscience* **21**, 1318–1331 (2018).
1130 24. Xiong, B. *et al.* Precise Cerebral Vascular Atlas in Stereotaxic Coordinates of Whole Mouse
1131 Brain. *Frontiers in Neuroanatomy* **11**, 128 (2017).
1132 25. Kirst, C. *et al.* Mapping the Fine-Scale Organization and Plasticity of the Brain Vasculature
1133 Resource Mapping the Fine-Scale Organization and Plasticity of the Brain Vasculature.
1134 *Cell* 1–16 (2020) doi:10.1016/j.cell.2020.01.028.
1135 26. Todorov, M. I. *et al.* Machine learning analysis of whole mouse brain vasculature. *Nature*
1136 *Methods* **17**, 442–449 (2020).
1137 27. Ji, X. *et al.* Brain microvasculature has a common topology with local differences in
1138 geometry that match metabolic load. *Neuron* **109**, 1168-1187.e13 (2021).
1139 28. Bennett, H. C. & Kim, Y. Advances in studying whole mouse brain vasculature using high-
1140 resolution 3D light microscopy imaging. *NPh* **9**, 021902 (2022).

1141 29. Wu, Y. *et al.* Quantitative relationship between cerebrovascular network and neuronal cell
1142 types in mice. *Cell Reports* **39**, (2022).
1143 30. Flurkey, K., M. Currer, J. & Harrison, D. E. Chapter 20 - Mouse Models in Aging Research.
1144 in *The Mouse in Biomedical Research (Second Edition)* (eds. Fox, J. G. et al.) 637–672
1145 (Academic Press, 2007). doi:10.1016/B978-012369454-6/50074-1.
1146 31. Blinder, P. *et al.* The cortical angiome: an interconnected vascular network with
1147 noncolumnar patterns of blood flow. *Nat Neurosci* **16**, 889–897 (2013).
1148 32. Tsai, P. S. *et al.* Correlations of Neuronal and Microvascular Densities in Murine Cortex
1149 Revealed by Direct Counting and Colocalization of Nuclei and Vessels. *Journal of*
1150 *Neuroscience* **29**, 14553–14570 (2009).
1151 33. Liwang, J. K., Bennett, H. C., Pi, H.-J. & Kim, Y. Protocol for using serial two-photon
1152 tomography to map cell types and cerebrovasculature at single-cell resolution in the whole
1153 adult mouse brain. *STAR Protoc* **4**, 102048 (2023).
1154 34. Wang, Q. *et al.* The Allen Mouse Brain Common Coordinate Framework: A 3D Reference
1155 Atlas. *Cell* **181**, 936-953.e20 (2020).
1156 35. Maheswaran, S. *et al.* Longitudinal regional brain volume changes quantified in normal
1157 aging and Alzheimer's APP x PS1 mice using MRI. *Brain Res* **1270**, 19–32 (2009).
1158 36. Berthiaume, A.-A. *et al.* Pericyte remodeling is deficient in the aged brain and contributes to
1159 impaired capillary flow and structure. *Nat Commun* **13**, 5912 (2022).
1160 37. Stamenkovic, S. *et al.* Impaired drainage through capillary-venous networks contributes to
1161 age-related white matter loss. 2024.02.11.579849 Preprint at
1162 https://doi.org/10.1101/2024.02.11.579849 (2024).

1163 38. Brown, L. S. *et al.* Pericytes and Neurovascular Function in the Healthy and Diseased Brain.
1164 *Front. Cell. Neurosci.* **13**, 282 (2019).
1165 39. Berthiaume, A. A. *et al.* Dynamic Remodeling of Pericytes In Vivo Maintains Capillary
1166 Coverage in the Adult Mouse Brain. *Cell Reports* **22**, 8–16 (2018).
1167 40. Cuttler, A. S. *et al.* Characterization of Pdgfrb-Cre transgenic mice reveals reduction of
1168 ROSA26 reporter activity in remodeling arteries. *Genesis (New York, N.Y. : 2000)* **49**, 673–
1169 680 (2011).
1170 41. Hartmann, D. A., Underly, R. G., Watson, A. N. & Shih, A. Y. A murine toolbox for
1171 imaging the neurovascular unit. *Microcirculation (New York, N.Y. : 1994)* **22**, 168–182
1172 (2015).
1173 42. Alheid, G. F. Extended amygdala and basal forebrain. *Ann N Y Acad Sci* **985**, 185–205
1174 (2003).
1175 43. Sato, A., Sato, Y. & Uchida, S. Regulation of cerebral cortical blood flow by the basal
1176 forebrain cholinergic fibers and aging. *Autonomic Neuroscience* **96**, 13–19 (2002).
1177 44. Ballinger, E. C., Ananth, M., Talmage, D. A. & Role, L. W. Basal Forebrain Cholinergic
1178 Circuits and Signaling in Cognition and Cognitive Decline. *Neuron* **91**, 1199–1218 (2016).
1179 45. Zolnik, T. A. *et al.* Layer 6b Is Driven by Intracortical Long-Range Projection Neurons. *Cell*
1180 *Reports* **30**, 3492-3505.e5 (2020).
1181 46. Nikolakopoulou, A. M. *et al.* Pericyte loss leads to circulatory failure and pleiotrophin
1182 depletion causing neuron loss. *Nature Neuroscience* **22**, 1089–1098 (2019).
1183 47. Trache, A., Massett, M. P. & Woodman, C. R. Vascular smooth muscle stiffness and its role
1184 in aging. in *Current Topics in Membranes* vol. 86 217–253 (Elsevier, 2020).

1185 48. Montero, D., Pierce, G. L., Stehouwer, C. D. A., Padilla, J. & Thijssen, D. H. J. The impact
1186 of age on vascular smooth muscle function in humans: *Journal of Hypertension* **33**, 445–
1187 453 (2015).
1188 49. Nishimura, N., Schaffer, C. B., Friedman, B., Lyden, P. D. & Kleinfeld, D. Penetrating
1189 arterioles are a bottleneck in the perfusion of neocortex. *Proc Natl Acad Sci U S A* **104**,
1190 365–370 (2007).
1191 50. Shih, A. Y. *et al.* Robust and fragile aspects of cortical blood flow in relation to the
1192 underlying angioarchitecture. *Microcirculation* **22**, 204–218 (2015).
1193 51. Ciurică, S. *et al.* Arterial Tortuosity. *Hypertension* **73**, 951–960 (2019).
1194 52. Weiss, D. *et al.* Mechanics-driven mechanobiological mechanisms of arterial tortuosity. *Sci*
1195 *Adv* **6**, eabd3574 (2020).
1196 53. Cai, C. *et al.* Impaired dynamics of precapillary sphincters and pericytes at first-order
1197 capillaries predict reduced neurovascular function in the aging mouse brain. *Nat Aging* **3**,
1198 173–184 (2023).
1199 54. Khan, U. A. *et al.* Molecular drivers and cortical spread of lateral entorhinal cortex
1200 dysfunction in preclinical Alzheimer's disease. *Nat Neurosci* **17**, 304–311 (2014).
1201 55. Van Hoesen, G. W., Hyman, B. T. & Damasio, A. R. Entorhinal cortex pathology in
1202 Alzheimer's disease. *Hippocampus* **1**, 1–8 (1991).
1203 56. Rodriguez, G. A., Burns, M. P., Weeber, E. J. & Rebeck, G. W. Young APOE4 targeted
1204 replacement mice exhibit poor spatial learning and memory, with reduced dendritic spine
1205 density in the medial entorhinal cortex. *Learning & Memory* **20**, 256–266 (2013).
1206 57. Alvarez, J. I. *et al.* The Hedgehog pathway promotes blood-brain barrier integrity and CNS
1207 immune quiescence. *Science* **334**, 1727–1731 (2011).

1208 58. Nyúl-Tóth, Á. *et al.* Demonstration of age-related blood-brain barrier disruption and
1209 cerebromicrovascular rarefaction in mice by longitudinal intravital two-photon microscopy
1210 and optical coherence tomography. *Am J Physiol Heart Circ Physiol* **320**, H1370–H1392
1211 (2021).
1212 59. Zhang, Q. *et al.* Cerebral oxygenation during locomotion is modulated by respiration. *Nature*
1213 *Communications* **10**, 1–15 (2019).
1214 60. Winder, A. T., Echagarruga, C., Zhang, Q. & Drew, P. J. Weak correlations between
1215 hemodynamic signals and ongoing neural activity during the resting state. *Nature*
1216 *Neuroscience* **20**, 1761–1769 (2017).
1217 61. Zhang, Q., Gheres, K. W. & Drew, P. J. Origins of 1/f-like tissue oxygenation fluctuations in
1218 the murine cortex. *PLOS Biology* **19**, (2021).
1219 62. Zhang, Q., Turner, K. L., Gheres, K. W., Hossain, M. S. & Drew, P. J. Behavioral and
1220 physiological monitoring for awake neurovascular coupling experiments: a how-to guide.
1221 *Neurophotonics* **9**, (2022).
1222 63. Huo, B.-X., Smith, J. B. & Drew, P. J. Neurovascular coupling and decoupling in the cortex
1223 during voluntary locomotion. *Journal of Neuroscience* **34**, 10975–10981 (2014).
1224 64. Drew, P. J. *et al.* Chronic optical access through a polished and reinforced thinned skull. *Nat*
1225 *Methods* **7**, 981–984 (2010).
1226 65. Drew, P. J., Shih, A. Y. & Kleinfeld, D. Fluctuating and sensory-induced vasodynamics in
1227 rodent cortex extend arteriole capacity. *Proc Natl Acad Sci U S A* **108**, 8473–8 (2011).
1228 66. Hillman, E. M. Coupling mechanism and significance of the BOLD signal: a status report.
1229 *Annu Rev Neurosci* **37**, 161–81 (2014).

1230 67. Ma, Y. *et al.* Wide-field optical mapping of neural activity and brain haemodynamics:
1231 considerations and novel approaches. *Philos Trans R Soc Lond B Biol Sci* **371**, (2016).
1232 68. Huo, B. X., Gao, Y. R. & Drew, P. J. Quantitative separation of arterial and venous cerebral
1233 blood volume increases during voluntary locomotion. *Neuroimage* **105**, 369–79 (2015).
1234 69. Vazquez, A. L., Fukuda, M., Crowley, J. C. & Kim, S.-G. Neural and Hemodynamic
1235 Responses Elicited by Forelimb- and Photo-stimulation in Channelrhodopsin-2 Mice:
1236 Insights into the Hemodynamic Point Spread Function. *Cerebral cortex (New York, N.Y. :*
1237 *1991)* **24**, 2908–2919 (2014).
1238 70. Tian, P. *et al.* Cortical depth-specific microvascular dilation underlies laminar differences in
1239 blood oxygenation level-dependent functional MRI signal. *Proc Natl Acad Sci U S A* **107**,
1240 15246–51 (2010).
1241 71. Longden, T. A. *et al.* Capillary K+-sensing initiates retrograde hyperpolarization to increase
1242 local cerebral blood flow. *Nat Neurosci* **20**, 717–726 (2017).
1243 72. Rungta, R. L., Chaigneau, E., Osmanski, B.-F. & Charpak, S. Vascular
1244 Compartmentalization of Functional Hyperemia from the Synapse to the Pia. *Neuron* **99**,
1245 362-375.e4 (2018).
1246 73. Rungta, R. L. *et al.* Diversity of neurovascular coupling dynamics along vascular arbors in
1247 layer II/III somatosensory cortex. *Commun Biol* **4**, 855 (2021).
1248 74. Bergel, A. *et al.* Adaptive modulation of brain hemodynamics across stereotyped running
1249 episodes. *Nat Commun* **11**, 6193 (2020).
1250 75. Cardoso, M. M., Sirotin, Y. B., Lima, B., Glushenkova, E. & Das, A. The neuroimaging
1251 signal is a linear sum of neurally distinct stimulus- and task-related components. *Nat*
1252 *Neurosci* **15**, 1298–306 (2012).

1253 76. Drew, P. J. Vascular and neural basis of the BOLD signal. *Curr Opin Neurobiol* **58**, 61–69
1254 (2019).
1255 77. Boas, D. A. & Franceschini, M. A. Haemoglobin oxygen saturation as a biomarker: the
1256 problem and a solution. *Philos Trans A Math Phys Eng Sci* **369**, 4407–24 (2011).
1257 78. Lyons, D. G., Parpaleix, A., Roche, M. & Charpak, S. Mapping oxygen concentration in the
1258 awake mouse brain. *Elife* **5**, (2016).
1259 79. Pandya, V. A. & Patani, R. Region-specific vulnerability in neurodegeneration: lessons from
1260 normal ageing. *Ageing Res Rev* **67**, 101311 (2021).
1261 80. Erdő, F., Denes, L. & de Lange, E. Age-associated physiological and pathological changes at
1262 the blood-brain barrier: A review. *J Cereb Blood Flow Metab* **37**, 4–24 (2017).
1263 81. Zimmerman, B., Rypma, B., Gratton, G. & Fabiani, M. Age-related changes in
1264 cerebrovascular health and their effects on neural function and cognition: A comprehensive
1265 review. *Psychophysiology* **58**, e13796 (2021).
1266 82. Lowerison, M. R. *et al.* Aging-related cerebral microvascular changes visualized using
1267 ultrasound localization microscopy in the living mouse. *Sci Rep* **12**, 619 (2022).
1268 83. Gunning-Dixon, F. M., Brickman, A. M., Cheng, J. C. & Alexopoulos, G. S. Aging of
1269 Cerebral White Matter: A Review of MRI Findings. *Int J Geriatr Psychiatry* **24**, 109–117
1270 (2009).
1271 84. Fulop, G. A. *et al.* Role of age-related alterations of the cerebral venous circulation in the
1272 pathogenesis of vascular cognitive impairment. *American Journal of Physiology-Heart and*
1273 *Circulatory Physiology* **316**, H1124–H1140 (2019).
1274 85. Sun, Z. *et al.* Age-Related Tortuosity of Carotid and Vertebral Arteries: Quantitative
1275 Evaluation With MR Angiography. *Frontiers in Neurology* **13**, (2022).

1276 86. Oliveros, E. *et al.* Hypertension in older adults: Assessment, management, and challenges.
1277 *Clin Cardiol* **43**, 99–107 (2019).
1278 87. Schager, B. & Brown, C. E. Susceptibility to capillary plugging can predict brain region
1279 specific vessel loss with aging. *J Cereb Blood Flow Metab* **40**, 2475–2490 (2020).
1280 88. Hoerder-Suabedissen, A. *et al.* Subset of Cortical Layer 6b Neurons Selectively Innervates
1281 Higher Order Thalamic Nuclei in Mice. *Cereb Cortex* **28**, 1882–1897 (2018).
1282 89. Hoyer, D. & Jacobson, L. H. Orexin in sleep, addiction and more: Is the perfect insomnia
1283 drug at hand? *Neuropeptides* **47**, 477–488 (2013).
1284 90. Nixon, J. P. *et al.* Sleep disorders, obesity, and aging: the role of orexin. *Ageing Res Rev* **20**,
1285 63–73 (2015).
1286 91. Zaborszky, L. *et al.* Specific Basal Forebrain-Cortical Cholinergic Circuits Coordinate
1287 Cognitive Operations. *Journal of Neuroscience* **38**, 9446–9458 (2018).
1288 92. Li, X. *et al.* Generation of a whole-brain atlas for the cholinergic system and mesoscopic
1289 projectome analysis of basal forebrain cholinergic neurons. *Proceedings of the National*
1290 *Academy of Sciences* **115**, 415–420 (2018).
1291 93. Grothe, M. *et al.* Reduction of basal forebrain cholinergic system parallels cognitive
1292 impairment in patients at high risk of developing Alzheimer's disease. *Cerebral cortex*
1293 *(New York, NY : 1991)* **20**, 1685–1695 (2010).
1294 94. Fischer, V. W., Siddiqi, A. & Yusufaly, Y. Altered angioarchitecture in selected areas of
1295 brains with Alzheimer's disease. *Acta Neuropathol* **79**, 672–679 (1990).
1296 95. Casu, M. A., Pan Wong, T., De Koninck, Y., Ribeiro-da-Silva, A. & Cuello, A. C. Aging
1297 Causes a Preferential Loss of Cholinergic Innervation of Characterized Neocortical
1298 Pyramidal Neurons. *Cerebral Cortex* **12**, 329–337 (2002).

1299 96. Sagare, A. P. *et al.* Pericyte loss influences Alzheimer-like neurodegeneration in mice.
1300 *Nature Communications* **4**, (2013).
1301 97. Zhang, X. *et al.* High-resolution mapping of brain vasculature and its impairment in the
1302 hippocampus of Alzheimer's disease mice. *National Science Review* **6**, 1223–1238 (2019).
1303 98. Taylor, E. N. *et al.* The brains of aged mice are characterized by altered tissue diffusion
1304 properties and cerebral microbleeds. *J Transl Med* **18**, 277 (2020).
1305 99. Haas, C. F., Loik, P. S. & Gay, S. E. Airway clearance applications in the elderly and in
1306 patients with neurologic or neuromuscular compromise. *Respir Care* **52**, 1362–81;
1307 discussion 1381 (2007).
1308 100. Schulte, H., Muhlfeld, C. & Brandenberger, C. Age-Related Structural and Functional
1309 Changes in the Mouse Lung. *Front Physiol* **10**, 1466 (2019).
1310 101. Korkushko, O. V., Ivanov, L. A., Pisaruk, A. V. & Chebotarev, N. D. The respiratory
1311 function of blood in elderly and old age and the factors that determine it. *Human*
1312 *Physiology* **35**, 163–169 (2009).
1313 102. Haberman, R. P., Koh, M. T. & Gallagher, M. Heightened cortical excitability in aged
1314 rodents with memory impairment. *Neurobiol Aging* **54**, 144–151 (2017).
1315 103. Fischer, C. *et al.* Prevention of age-associated neuronal hyperexcitability with improved
1316 learning and attention upon knockout or antagonism of LPAR2. *Cell Mol Life Sci* **78**, 1029–
1317 1050 (2021).
1318 104. Popescu, I. R. *et al.* Increased intrinsic excitability and decreased synaptic inhibition in
1319 aged somatosensory cortex pyramidal neurons. *Neurobiol Aging* **98**, 88–98 (2021).

1320 105. Harb, R., Whiteus, C., Freitas, C. & Grutzendler, J. In vivo imaging of cerebral
1321 microvascular plasticity from birth to death. *J Cereb Blood Flow Metab* **33**, 146–156
1322 (2013).
1323 106. Kapasi, A. *et al.* Watershed Microinfarct Pathology and Cognition in Older Persons.
1324 *Neurobiol Aging* **70**, 10–17 (2018).
1325 107. Shin, P. *et al.* Aerobic exercise reverses aging-induced depth-dependent decline in cerebral
1326 microcirculation. *eLife* **12**, e86329 (2023).
1327 108. Wang, T. *et al.* Three-photon imaging of mouse brain structure and function through the
1328 intact skull. *Nat Methods* **15**, 789–792 (2018).
1329 109. Brunner, C. *et al.* Whole-brain functional ultrasound imaging in awake head-fixed mice.
1330 *Nat Protoc* **16**, 3547–3571 (2021).
1331 110. Grant, R. I. *et al.* Organizational hierarchy and structural diversity of microvascular
1332 pericytes in adult mouse cortex. *Journal of Cerebral Blood Flow and Metabolism* **39**, 411–
1333 425 (2019).
1334 111. Gao, Y. R. & Drew, P. J. Effects of Voluntary Locomotion and Calcitonin Gene-Related
1335 Peptide on the Dynamics of Single Dural Vessels in Awake Mice. *J Neurosci* **36**, 2503–16
1336 (2016).
1337 112. Gehrmann, J. *et al.* Phenotypic screening for heart rate variability in the mouse. *Am J*
1338 *Physiol Heart Circ Physiol* **279**, H733-40 (2000).
1339 113. Boynton, G. M., Engel, S. A., Glover, G. H. & Heeger, D. J. Linear systems analysis of
1340 functional magnetic resonance imaging in human V1. *J Neurosci* **16**, 4207–21 (1996).
1341 114. Glover, G. H. Deconvolution of impulse response in event-related BOLD fMRI.
1342 *Neuroimage* **9**, 416–29 (1999).

1343 115. Madsen, M. T. A simplified formulation of the gamma variate function. *Phys Med Biol* **37**,
1344 1597–1600 (1992).
1345 116. Cohen, M. S. Parametric analysis of fMRI data using linear systems methods. *Neuroimage*
1346 **6**, 93–103 (1997).
1347 117. Sirotin, Y. B. & Das, A. Anticipatory haemodynamic signals in sensory cortex not
1348 predicted by local neuronal activity. *Nature* **457**, 475–9 (2009).
1349 118. Yu, X., Qian, C., Chen, D. Y., Dodd, S. J. & Koretsky, A. P. Deciphering laminar-specific
1350 neural inputs with line-scanning fMRI. *Nat Methods* **11**, 55–8 (2014).
1351 119. Korogod, N., Petersen, C. C. & Knott, G. W. Ultrastructural analysis of adult mouse
1352 neocortex comparing aldehyde perfusion with cryo fixation. *Elife* **4**, (2015).

1353
1354
1355